A Procedure for the Generation of Material for Flat-Joint Models and the Simulation of Rock Testing using PFC2D

A Thesis

Presented in Partial Fulfillment of the Requirements for the

Degree of Master of Science

with a

Major in Geological Engineering

in the

College of Graduate Studies

University of Idaho

by

Lapone Techapinyawat

Major Professor: S.J. Jung, Ph.D.

Committee Members: Sunil Sharma, Ph.D.; Ahmed A. Ibrahim, Ph.D.

Department Administrator: Fritz R. Fiedler, Ph.D.

August 2021

Authorization to Submit Thesis

This thesis of Lapone Techapinyawat, submitted for the degree of Master of Science with a Major in Geological Engineering and titled " A Procedure for the Generation of Material for Flat-Joint Models and the Simulation of Rock Testing using PFC2D," has been reviewed in final form. Permission, as indicated by the signatures and dates below, is now granted to submit final copies to the College of Graduate Studies for approval.

Major Professor: _____ Date: _____

S.J. Jung, Ph.D.

Committee Members: _____ Date: _____

Sunil Sharma, Ph.D.

_____ Date: _____

Ahmed A. Ibrahim, Ph.D.

Department Administrator: _____ Date: _____

Fritz R. Fiedler, Ph.D.

Abstract

The overall behavior of rock mass is effectively controlled by the micro properties of its constituent particles and the bonds between the particles. Unfortunately, the micro-scale properties are difficult to measure with routine laboratory tests. This study, using Discrete Element Methods (DEM), investigated the influence of these micro-scale bonding properties on typical parameters which may be measured in a uniaxial compression test.

This research used the DEM software: “PFC2D” (Itasca 2019) to investigate the influence of the micro-scale bond properties. PFC2D is a popular DEM simulation program that can be used to study the behavior of rock made up of discrete particles. It creates discontinuous bodies, balls, clusters, and clumps in the model and bonds them together as a rigid body. However, the material properties to be assigned in the model are bond properties, and not typical material properties. “Inverse modeling" is used to essentially back-calculate appropriate bond properties that will match laboratory material properties. Calibrating the material without studying the consequence of assigning bond parameters is not practical. So, this research provided a parametric study of four bond parameters: (1) normal to shear stress ratio (kratio), (2) tensile strength (fj_ten), (3) effective modulus (emod), and (4) cohesion (fj_coh). The parameter labels, such as kratio, correspond to the names defined for use in PFC2D. These selected parameters were varied for a total of 108 uniaxial compressive and 108 direct tension simulations to see which parameters should be adjusted and calibrated first to match lab tests.

The recommended procedure for generating material for flat-joint models starts with adjusting the four bond parameters in the following preferred order: (1) kratio to match the material's, Poisson's ratio, (2) fj_ten to match the material's tensile strength, (3) emod to match the material's Young's modulus, and (4) fj_coh to match the material's compressive strength.

This procedure was found to be most effective because the last parameter's calibration does not affect the previously calibrated parameters. The bond's friction angle was assumed to equal the material's friction angle for all cases.

Because the calibrated, simulated material behaves identically to the real specimen, the development of cracks during loading was also studied. Interestingly, the study demonstrates that the material cracks in a small portion of the linear elastic zone before entering the nonlinear zone.

Additionally, we discovered that the inclusion of rock lineations, with different properties, resulted in a range of compressive strength, Young's modulus, and ultimate axial strain, depending on the angles. The compressive strength, Young's modulus, and axial strain of materials with lineation acting at a 30-degree angle to the maximum principal stress produced the lowest values.

Key Words: Bond parameters, DEM, Discrete elements, Macro properties, Micro properties, PFC, PFC2D, Rock properties, Rock testing, Simulation.

Acknowledgements

I have received excellent support from many people while pursuing a master's degree at the University of Idaho and conducting research.

First, I would like to express my heartfelt appreciation to my major professor, S.J. Jung, for guiding me throughout my two-year study and supervising the research track, and providing constructive feedback on my work. Second, I am indebted to Professor Patricia J. S. Colberg for her support. Thirdly, I would like to express my gratitude to the thesis committee members, Dr. Sunil Sharma and Dr. Ahmed Ibrahim, for taking the time to review my thesis.

It has been a difficult time during the COVID-19 pandemic, but the support of everyone around me has made these years valuable.

Dedication

I would like to express my gratitude to all of my family members

for their support as I pursue a higher degree in the United States of America,

despite our geographical separation.

We have not met in nearly two years due to the COVID-19 pandemic, but they attempt to

contact me almost every night.

Thanks, dad, mom, and sisters!

Table of Contents

List of Tables

List of Figures

Chapter 1: Introduction

1.1 Overview

For geological and geotechnical designs, engineers must contend with the fact that rock and soil are unique materials, consisting of discrete particles with complex properties at the micro scale. The extent and variability of these properties and their influence on overall mass behavior must be recognized and then simplified for analysis and design.

For example, a rock slope will have different properties along joints and fissures compared to the intact mass. Additionally, the slope may have a complex structure, with a non-planar slope face, rock folding, complicated joint pattern, and varying hardness and weathering of each stratum. The stability of such slopes is very difficult to assess using established principles of engineering mechanics due to complex nature of the properties.

As an example, Figure 1.1 shows the face of a rock quarry in Thailand. The quarry's slope face is non-planar and has a variable slope angle. Additionally, the rock exhibits a chevron folding structure, with the left flank being steeper than the right flank. Due to the site's variation in all three dimensions, engineers may be wondering where the exact location of the failure will be, which plane will be fail, which direction the rock will fall, and how large it will be? Such evaluations are difficult to perform analytically as many parameters have to be assigned with the slope model.

Figure 1.1 Slope face of a rock quarry in Thailand. The dashed white lines denote the bedding planes.

Due to the complexity of rock mass, geological engineers frequently use simulation to solve problems and design structures. The finite element method (FEM) and the discrete element method (DEM) are the most commonly used numerical methods in geomaterials modeling. However, each simulation technique has its advantages and disadvantages. For example, FEM is appropriate for macroscale, continuous media, whereas DEM is appropriate for microscale studies.

The discrete element method (DEM) is a particle-scale numerical method for simulating discontinuous bodies consisting of many rigid or deformable particles. These particles will be simulated by discs in the two-dimensional domain and spherical balls in the three-dimensional domain. Because the model's elements are discontinuous bodies, scientists and engineers can use this method to study the mechanical behavior of granular materials in the real world. For example, DEM can estimate the depositional or erosional rate of bedload gravel in a high-

flow channel. It can illustrate soil scouring at riverbed bridge piers. Interestingly, we can use DEM to create rock masses because sedimentary rocks are composed of granular materials, whereas igneous and metamorphic rocks are composed of crystalline materials. Figure 1.2 shows a graphite schist thin section under a polarized microscope; this is the example of foliated metamorphic rock that contains many types of mineral crystalline. We can assume each mineral crystalline is one discontinuous body in the DEM for a basic model, and by assembling numerous discontinuous bodies, we can synthesize an entire piece of a rock mass.

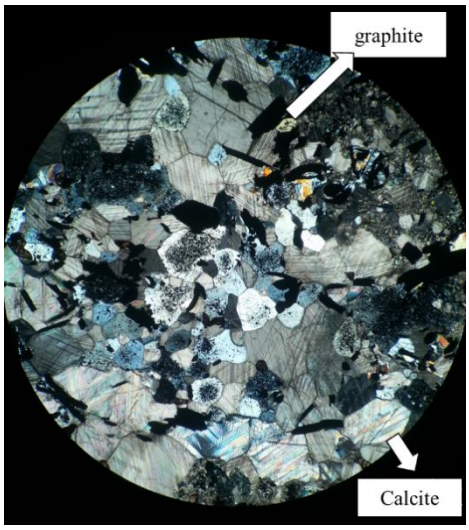

Figure 1.2 Graphite schist under polarized microscope.

1.2 Particle Flow Code

Particle Flow Code (PFC) is a multipurpose discrete element-based model software that simulates the movement and interaction of many particles of finite size. The PFC software from Itasca Consulting used in this study is the 2D version, PFC6.0. It can use geomechanics research to analyze and visualize a model graphically or specify fundamental rigid body theories such as Newton's equations of motion.

However, because this program is based on the DEM, there are some difficulties in creating materials for the simulation. While the FEM material property assignment can be specified in

the program using values obtained from laboratory experiments, the DEM material property assignment is not as straightforward as the FEM because the input values are not equal to laboratory material properties. That is because the input properties of the DEM are for discontinuous bodies, not solid materials. The PFC6.0 software documentation states that “while it is easy to assign selected attributes and properties to a PFC model, it is difficult to select such parameters to represent an actual material accurately.”

PFC derives its behavior at a more fundamental level from the material's micro-components (equivalent grains and interfaces). It is the mechanical properties of these grains, interfaces and shapes that are used as input to PFC. The term "direct modeling" refers to this approach. However, if we simulate a solid, such as a rock, we may be unaware of the microscopic constituents' mechanical properties. In this instance, it is essential to apply "inverse modeling." Once a suitable match is discovered, the appropriate set of parameters may be used for the entire simulation. This process is illustrated in Figure 1.3.

Figure 1.3 shows the flow chart to model sample behavior. The first step is model setup. This step includes generating balls according to defined distribution, assigning the ball's radius, and bond properties. Then, the second step is waiting for the model to reach equilibrium, which means that the balls have stopped moving. The third and final step examines the model

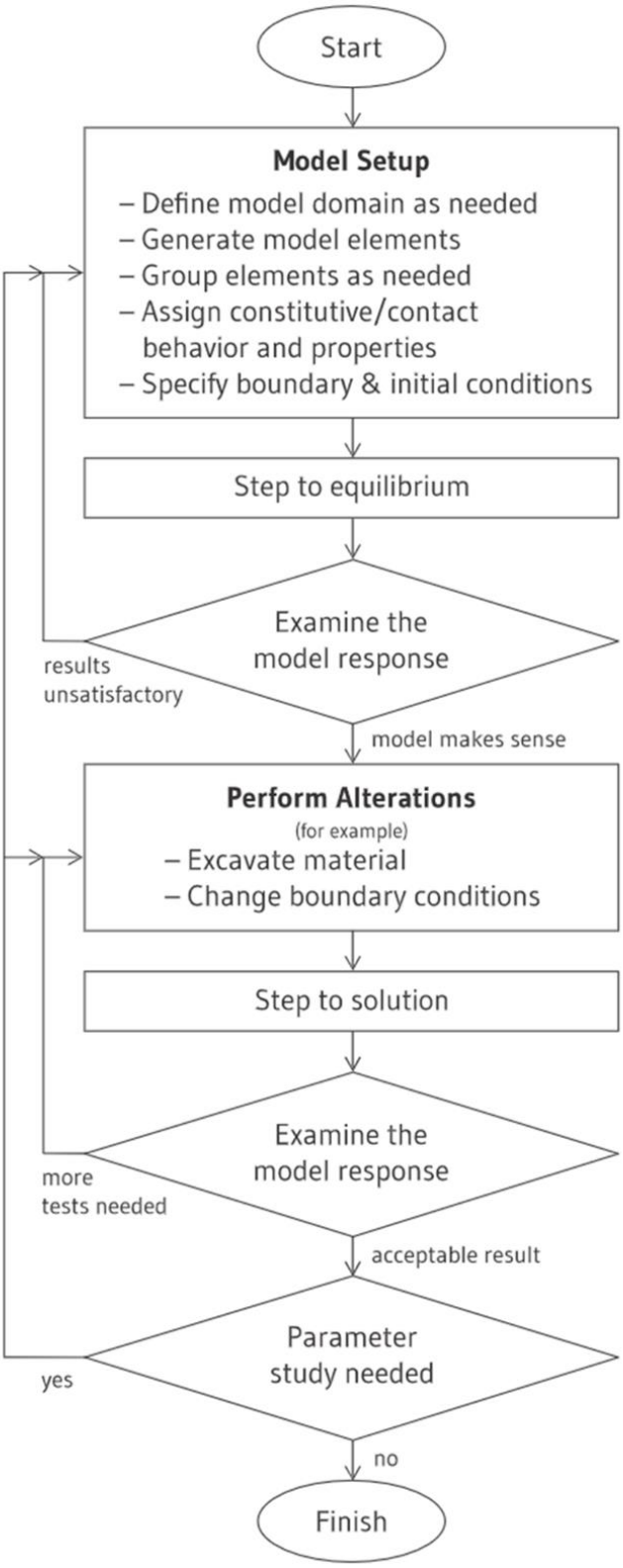

Figure 1.3 Flowchart of the complete simulation process in PFC6.0.

response. This step can be done by imitating the actual experiment. For example, uniaxial compressive simulation is used to investigate the compressive strength of the model. If the model response does not make sense, the calibration must go back to step one to change the contact properties and repeat the process. Once a match is discovered, the appropriate set of parameters may be used for the entire simulation

1.3 Problem Statement and Objectives

Inverse modeling is used in an iterative process to assign contact properties to the discontinuous bodies until the macroscopic behavior of the solid model is simulated effectively. If the initial contact properties fail to effectively simulate the behavior of the solid model, the properties are adjusted repeatedly until the correct response is achieved. The method used to examine the PFC model response is similar to laboratory experiments; for example, the uniaxial compressive simulation could be used to mimic the uniaxial compressive test used to determine compressive strength, Young's modulus, and Poisson's ratio.

The computation time to complete the calibration process takes longer when the simulated material properties do not match the solid material: one simulation could take more than one hour. Each input parameter in the PFC model has a direct affect on more than one simulated material property. As program users need to calibrate these parameters iteratively, this stage often take considerably more time if the final model is to be used to observe fracture development in projects such as the tunneling excavation.

The objectives of this study focus on the parametric study assigned to PFC2D and to develop an easy-to-use material genesis procedure that minimizes the time required for calibration and accuracy. The developed procedure generates material properties for use in PFC2D that are identical to those of the actual rock sample with less than 1% of property error. The author believes that performing DEM simulations should be focused on the final goal, not the calibration process. Additionally, simulated material properties should closely resemble those of the actual rock sample, because otherwise, the final interpretation of the simulation may be incorrect.

Additionally, following the development of an easy-to-use material genesis procedure, the study examines the simulated material's behavior to determine the compressive strength and damage development of homogeneous and heterogeneous rocks subjected to compressive loads that laboratory experiments cannot monitor. Damage development is further described in detail in Chapter 4.

1.4 Research Tasks

The above objectives were achieved by completing the following tasks:

Task 1: Conduct Literature Review

The author conducted a thorough review of the literature and provided background on the DEM's fundamental governing equations and a review of the PFC's built-in contact model and whether it should generate a rock sample on the PFC. Additionally, the author discusses the contact mechanisms between two discontinuous bodies (two-dimensional discs) to develop a material genesis procedure.

Task 2: Conduct a parametric study using PFC6.0

The author investigates the effect of microscopic input parameters (bond properties) on macroscopic (material) properties such as compressive strength, tensile strength, and Young's modulus in this task by varying four bond properties to generate 108 different simulated samples. Compressive stimulation and tension simulations with 108 samples are used to observe the material response.

Task 3: Establish a procedure for material genesis and its validation

We can observe the effect of bond properties on material properties once task 3 is completed. As a result, we use observation to determine which micro parameters should be assigned and calibrated first to match the material property and which should be adjusted last. The author then performed laboratory experiments on example samples to validate the procedure.

Task 4: Geomechanics applications of the PFC6.0

In this task, we use the benefits of the PFC6.0 to create materials that are difficult to obtain naturally, as the PFC6.0 can remove or minimize properties in the materials that affect the laboratory test results; for example, the PFC6.0's ability to generate and control the mineral content in the simulated rock. Simultaneously, obtaining actual rock samples with the required mineral content is difficult. Additionally, the PFC6.0 observes microcrack development, which is challenging to do in a laboratory experiment.

1.5 Organization of the Study

Chapter 1 presents an overview and introduction to the use of DEM. It also covers the research effort, including the problem statement and objectives, the research tasks, and the study organization.

Chapter 2 provides a review of the literature on DEM. It also includes a brief summary of the basic governing equations used by DEM, and provides details of the PFC's built-in contact model mechanism.

Chapter 3 demonstrates the process adopted to conduct a parametric study and how each input parameter responds to the material behavior. Additionally, this chapter covers establishing a procedure for the genesis of material and its validation, covering Tasks 2 and 3.

Chapter 4 discusses the applications of the 2D PFC6.0 software to simulate homogeneous and heterogeneous materials for geomechanics studies. It also provides details and results of the simulations performed for cases withlineations (inclusions) oriented at different angles within the sample.

Chapter 5 summarizes all of this research, provides conclusions, and makes recommendations for future research.

The Appendix at the end of this thesis includes a summary of the bond properties used for the simulations.

Chapter 2: Literature Review

The discrete element method (DEM) has been recognized recently as an efficient numerical tool for solving a wide variety of scientific and technological problems in many engineering disciplines. Peter Cundall was one of the first researchers to present the DEM for simulating the movement of blocky rocks systems (Cundall, 1971). Then, Cundall and Strack (1979) extended DEM to study the dynamic behavior of granular medium. The granular medium comprises discrete particles that displace independently from one another and interact only at contact points. The interactions between discrete particles are controlled by microproperties. These microproperties consist of stiffness and strength parameters for the particles and the bonds (Potyondy & Cundall, 2004). In general, rock can be treated as a granular material whose micro-mechanical behavior is discontinuous (Ding, et. al., 2013).

The Particle Flow Codes (PFC2D and PFC3D) (Potyondy & Cundall, 2004) are among the most widely used DEM software. The basic idea of PFC is to treat rock as an assembly of bonded particles that follow the law of motion and consider the model behavior dominated by the formation and interaction of microcrack development (Potyondy & Cundall, 2004). An important aspect of PFC application is the assignment of microscopic model parameters. As the micro parameters are unknown and typically cannot be measured directly during laboratory experiments, they are frequently back calculated using numerical calibrations against macro property values determined during testing (Ding, et al., 2013).

Several researchers have investigated the relationship between micro and macro parameters. For example, Yoon (2007) studied the sensitivity of microparameters with respect to uniaxial compressive strength by Plackett–Burman (Plackett & Burman, 1946) and the more conventional Central Composite Design methods. Sun, et al., (2013) used a full factorial design procedure with help from an artificial neural network to map the macro parameters onto micro parameters in PFC3D. Further analyses were presented by Peng-Yu (2016), who used Analysis of Variance (ANOVA) of micro and macro parameters to reveal whether factors significantly affect the dependent parameters.

2.1 Governing DEM equations for rigid discontinuous bodies

The development of DEM techniques is primarily for studying the mechanical deformation/ motion processes of particle assemblages. DEM's fundamental principles are based on the equations of motion in a solid and continuum mechanics' general conservation equations for mass, momentum, and energy. Jing and Stephansson (2006) provide a summary of the concepts following this.

2.1.1 Newton's equations of motion for particles and rigid body

The definition of a discontinuous body is a constant mass. The momentum of a particle (p) that describe the dynamical behavior is the product of mass (m) and velocity (v) of a particle,

$$p_i = mv_i \qquad (i = 1, 2, 3, \dots) \tag{2.1}$$

According to Newton's second law, the resultant force (f) acting on the particle and causing it to move equals the rate at which its linear momentum changes. Because a particle's mass remains constant while it is in motion, the law can be expressed as,

$$f_i = \dot{p}_i = \frac{dp}{dt} = m\dot{v}_i = \frac{\mathrm{d}(mv_i)}{\mathrm{d}t} = m\frac{\mathrm{d}(v_i)}{\mathrm{d}t} = ma_i \tag{2.2}$$

2.1.2 Newton–Euler equations of motion

Volume (V) and mass (m) do not deform in rigid discontinuous bodies, and hence the distance between any two points in a rigid body remains constant. As a result, the dynamics of rigid bodies are regulated by Newton's law of motion and Euler's rotations of rigid bodies.

2.1.2.1 Moments and products of inertia

The moments and products of inertia of a rigid body are the most significant characteristics. Assume that dm is the mass of a differential element embedded in a rigid body. D$m = \rho \mathrm{d}V = \rho \mathrm{d}x\mathrm{d}y\mathrm{d}z$. Vector $\vec{\mathbf{r}} = \{r_i\} = (x, y, z)$ represents its position of mass i and $(l, m, n) = (\cos\alpha, \cos\beta, \cos\gamma)$

The moment of inertia of the element about axis OB shown in Figure 2.1 are

$$\mathrm{d}I_{OB} = \rho[(x^2 + y^2 + z^2)(l^2 + m^2 + n^2) - (lx + my + nz)^2]\mathrm{d}V \tag{2.3}$$

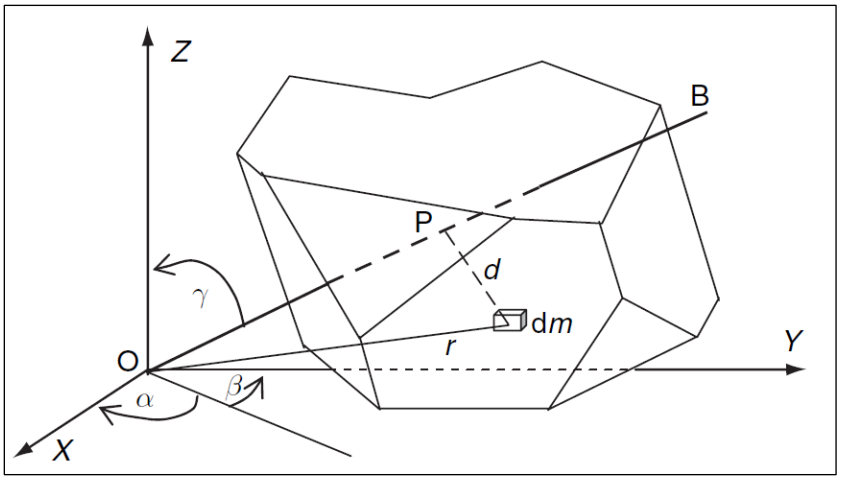

Figure 2.1 Moments of inertia of a rigid body about an arbitrary axis OB (Jing and Stephansson, 2006).

Therefore, the moments of inertia of a body are,

$$I\mathrm{OB} = \int \rho[l^2(y^2+z^2) + m^2(x^2+z^2) + n^2(x^2+y^2) - 2lm(xy) - 2\ln(xz) - 2mn(yz)]\mathrm{d}V$$
$$= \rho\left[l^2 I_{xx} + m^2 I_{yy} + n^2 I_{zz} - 2lmI_{xy} - 2lnI_{xz} - 2mnI_{yz}\right] \quad (2.4)$$

And the products of inertia of a rigid body is,

$$I_{ij} = \begin{bmatrix} I_{xx} & I_{xy} & I_{xz} \\ I_{yx} & I_{yy} & I_{yz} \\ I_{zx} & I_{zy} & I_{zz} \end{bmatrix} \quad (2.5)$$

2.1.2.2 Mass, linear, and angular moments

Mass (M) is defined by,

$$M = \iiint \rho \mathrm{d}V = \rho V \quad (2.6)$$

Linear momentum (p_i) is defined by,

$$p_i = \iiint p v_i \mathrm{d}V \quad (2.7)$$

Angular momentum (h_i) is defined by,

$$h_i = \iiint \rho(\vec{\mathbf{r}} \times \vec{\mathbf{v}}) dV \tag{2.8}$$

2.1.3 Euler's equations of rotational motion

Definition of angular momentum from equation (2.8), and writing $\dot{X} = v_x$, $\dot{Y} = v_y$, $\dot{Z} = v_z$. As velocity components, the basic form of Euler's rotational equations for a rigid body is specified in an inertial frame without angular velocity, moments, or inertia products. Where (T_X, T_Y, T_Z) are the torques generated by the applied external forces.

$$\begin{cases} \dot{h}_X = \frac{\mathrm{d}}{\mathrm{d}t}\int \rho(v_z Y - v_Y Z)\mathrm{d}V = \int \rho(f_z Y - f_Y Z)\mathrm{d}V = T_X \\ \dot{h}_Y = \frac{\mathrm{d}}{\mathrm{d}t}\int \rho(v_X Z - v_Z X)\mathrm{d}V = \int \rho(f_x Z - f_z X)\mathrm{d}V = T_Y \\ \dot{h}_Z = \frac{\mathrm{d}}{\mathrm{d}t}\int \rho(v_Y X - v_X Y)\mathrm{d}V = \int \rho\big(f_y X - f_x Y\big)\mathrm{d}V = T_Z \end{cases} \tag{2.9}$$

2.2 PFC Overview

A generic particle-flow model approximates the mechanical behavior of a collection of arbitrarily formed particles. The model consists of separate particles that move independently of one another and interact via pair-wise contacts. Newton's laws of motion establish a basic connection between the motion of particles and the forces. The PFC6.0 documentation defines the model's assumptions as follows: The PFC6.0 documentation defines the model's assumptions as follows:

1. Particles are considered rigid bodies.
2. Ball is the fundamental particle shape.
3. The clump logic supports the creation of rigidly attached, denoted pebbles. Each clump is formed by overlapping pebbles that function as a rigid body with a deformable boundary. Figure 2.2 explains the definition of model objects (ball, clump, pebble, and facet) in the PFC.
4. At pair-wise contacts, particles interact through an internal force and moment. Contact mechanics is represented in the laws of particle interaction that dynamically update internal forces and moments.

5. At particle-particle interfaces, bonds can form.

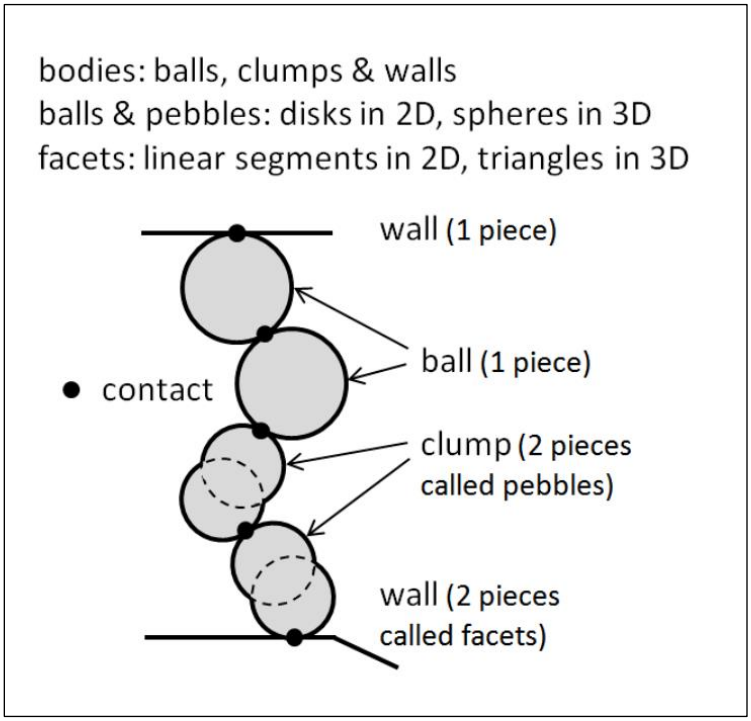

Figure 2.2 Type of discontinuous bodies in PFC6.0.

2.3 PFC Built-in contact models

PFC6.0 (released in 2019) includes 12 built-in contact models (Figure 2.3). Each built-in model is optimized for a specific simulation based on the ball-to-ball mechanisms. Linear contact bond, linear parallel bond, linear rolling resistance, and adhesive rolling resistance linear contact models are all linear-based models. Each linear-based model is composed of two groups: the Linear Group and the Dashpot Group. These contact models are used to create Bonded-Particle Models (BPM).

The methodology of bonded-particle modeling generates an enormous number of microstructural models in the form of bonded materials (Potyondy, 2019). A bonded material is described as a densely packed assemblage of rigid grains bonded together at grain-grain contacts by deformable and breakable cement (Figure 2.4). In a bonded material, damage occurs because of bond-breakage events, which is recognized as a crack.

Name	Behavior Summary
null	No mechanical interaction.
linear	Linear elastic, frictional and viscous behavior.
linear contact bond	Linear model and contact bonding for BPM.
linear parallel bond	Linear model and parallel bonding for BPM.
soft bond	Linear softening bond model for BPM or granular applications.
rolling resistance linear	Linear model and rolling-resistance mechanism for granular applications.
adhesive rolling resistance linear	Linear model, rolling-resistance mechanism and adhesion to give a cohesive granular material.
flat joint	Finite-size, linear elastic and either bonded or frictional interface with partial damage for BPM.
smooth joint	Provides a joint within a BPM.
hertz	Non-linear elastic, frictional and viscous behavior for granular applications including impact problems.
hysteretic	Similar to hertz model but for impact problems, directly specify normal restitution coefficient.
Burger's	Provides a creep mechanism for granular applications.

Figure 2.3 Built-in contact models in PFC6.0.

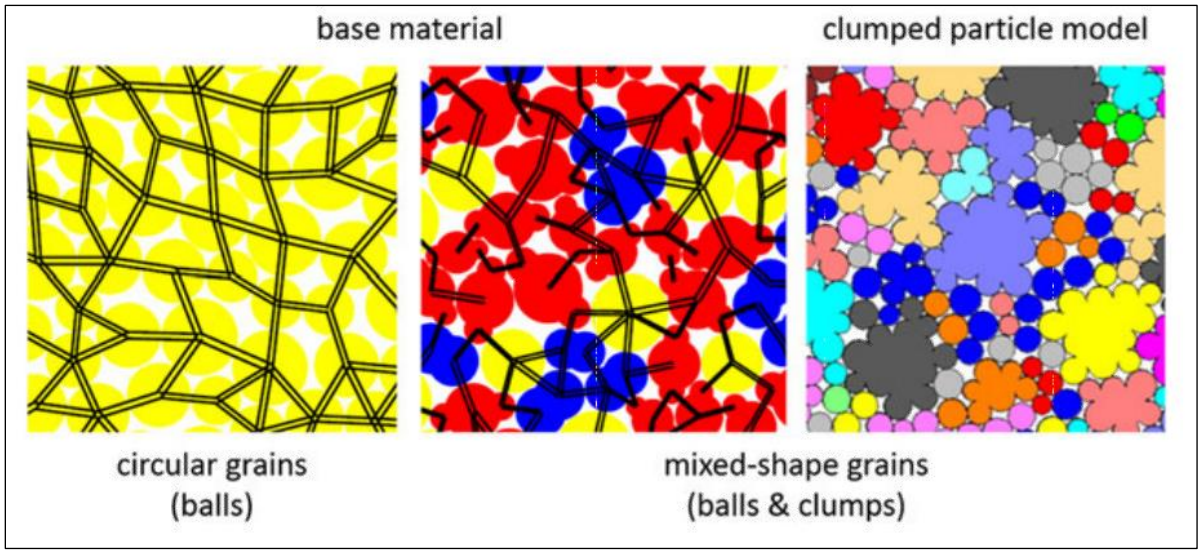

Figure 2.4 BPM base material consisting of balls and clumps. Cement drew as pairs of black lines (Yoon et al., 2012).

2.4 Flat-joint contact model in 2D

The flat-joint contact model describes the macroscopic behavior of a finite-size, linear elastic, bonded, or frictional surface that has sustained partial damage. The behavior of a bonded element is linear elastic until the strength limit is exceeded and the bond breaks, making the element unbonded. The behavior of an unbonded element is linearly elastic and frictional, with slip accommodated by imposing a Coulomb limit on the shear force (PFC6.0, 2019).

The mechanism that makes a flat-joint model unique from other built-in contact models creates a rectangular contact interface between ball and ball. This rectangular interface has a total width equal to the diameter of a ball (2R; where R is the ball's radius) and a depth of unit thickness. Each interface contains four "elements," as shown blue line in Figure 2.5. This interface length results in granular-shaped discontinuous bodies that mimic mineral crystals found in rocks, as illustrated in Figure 2.6. It can be compared to the rock shown under a polarized microscope in Figure 1.2.

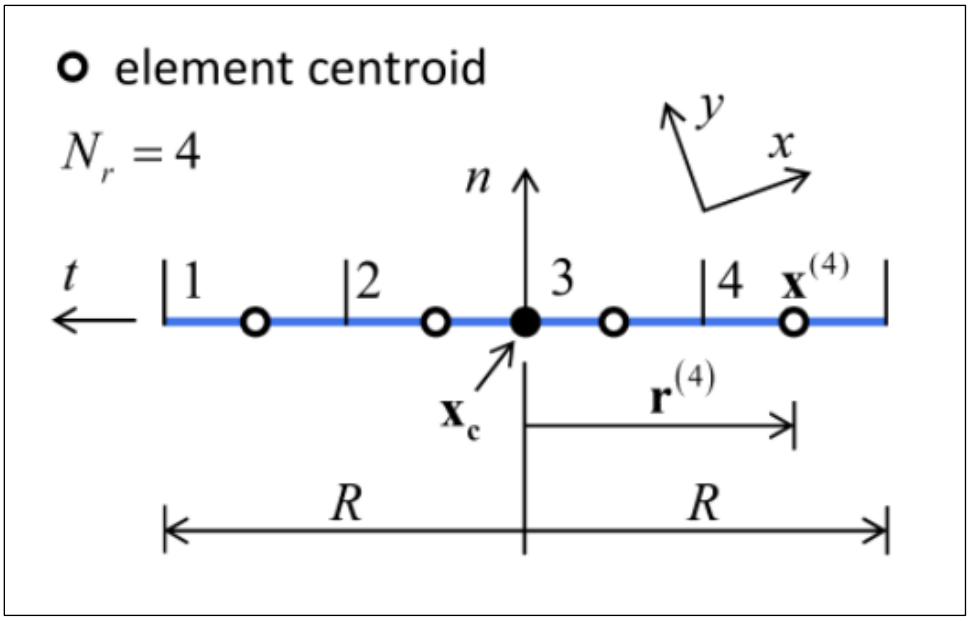

Figure 2.5 The interface discretization of a two-dimensional flat-joint model demonstrates the element-numbering convention (PFC6.0).

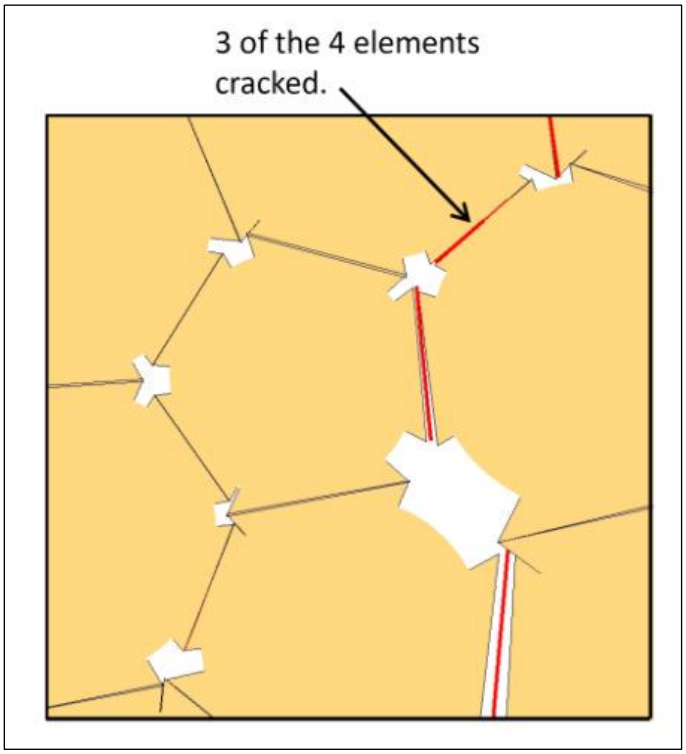

Figure 2.6 The interface between the balls in the flat-joint contact model is a black line, whereas a red line represents a bond crack (PFC6.0).

The area of each element ($A^{(e)}$), shown in Figure 2.5, is equal to

$$A^{(e)} = \frac{2Rt}{N_r} \tag{2.10}$$

While in the 2-dimensional domain, the number of elements (N_r) is equal to 4, and t is a depth of unit thickness (t=1). Therefore $A^{(e)}$ is

$$A^{(e)} = 0.5R \tag{2.11}$$

The centroid location of each element ($x^{(e)}$), shown in Figure 2.5, is equal to

$$x^{(e)} = x_c + r^{(e)}, \qquad \text{e = 1, 2, 3, 4} \tag{2.12}$$

Where

$$r^{(e)} = \rho^{(e)}\hat{\mathbf{t}}_c \tag{2.13}$$

$$\rho^{(e)} = R\left(\frac{-2e+1+N_r}{N_r}\right)$$

In 2D domain

$$\rho^{(e)} = R\left(\frac{-2e+5}{4}\right) \tag{2.14}$$

2.4.1 Force Displacement Law

According to PFC6.0, each element (one interface between balls contains four elements) carries a force ($F^{(e)}$) and moment ($M^{(e)}$) acting at the element centroid. The element forces and moments form a statically equal force ($\tilde{F}, F_c$) and moment ($\tilde{M}, M_c$) at the interface's center. Figure 2.7 shows the concept of forces and moments acting on an element and total force and moment at the centroid of the interface.

$$\tilde{F} = \sum_{\forall e} F^{(e)} \tag{2.15}$$

Where

$$F^{(e)} = -F_n^{(e)}\hat{\mathbf{n}}_c + F_s^{(e)} \tag{2.16}$$

$$\tilde{M} = \sum_{\forall e}\left\{\left(r^{(e)} \times F^{(e)}\right) + M^{(e)}\right\} \tag{2.17}$$

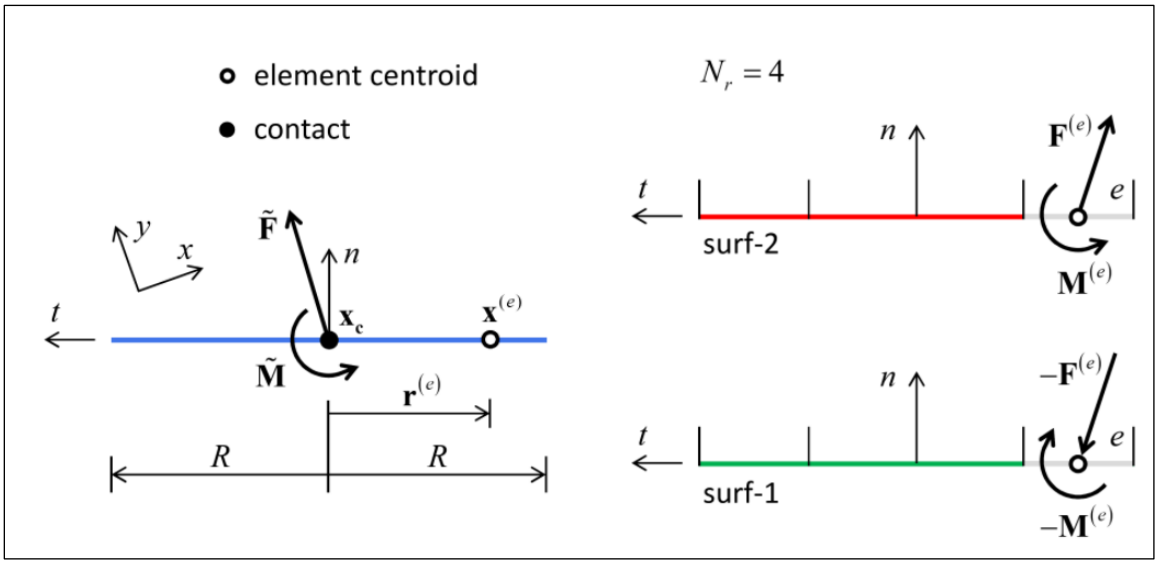

Figure 2.7 Schematic of centroid force and moment (left) and forces and moments are acting on an element (right) (PFC6.0).

Then element normal and shear stresses are

$$\sigma^{(e)} = \frac{F_n^{(e)}}{A^{(e)}} \tag{2.18}$$

$$\tau^{(e)} = \frac{F_s^{(e)}}{A^{(e)}} \tag{2.19}$$

2.4.2 Bonded and unbonded conditions

The flat-joint model's bonded and unbonded conditions simulate the cement's cracking mechanism between two crystalline surfaces. A bonded condition behaves identically to a fully joined cementation, whereas an unbonded condition behaves like damage or crack between two crystalline surfaces.

Bonded condition:

The behavior of a bonded element is linear elastic, controlled by normal stiffness (k_n) and shear stiffness (k_s) of the contact. The program user can specify these stiffnesses. As illustrated in Figure 2.8, both normal and shear stiffnesses directly affect the slope of the stress-displacement graph. Displacement refers to the normal ($g^{(e)}$) and tangential ($\delta^{(e)}$) distances between two balls.

Normal Stress; $$\sigma^{(e)} = k_n g^{(e)} \quad (2.20)$$

Shear stress; $$\tau^{(e)} = k_s \delta_s^{(e)} \quad (2.21)$$

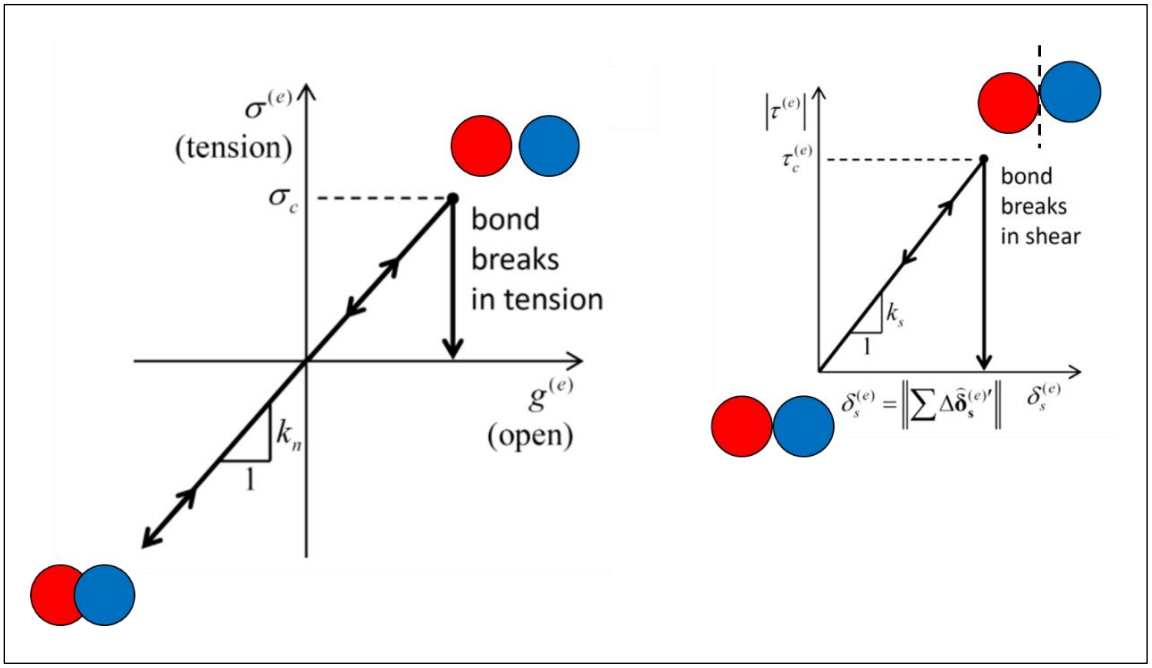

Figure 2.8 A bonded flat-joint element's force-displacement law. Normal stress in the normal direction (left) and shear stress in the tangential direction (right) vs. element gap (PFC6.0).

Normal stress or shear stress can both break the bond between two balls. When the normal stress on an element exceeds the bond's tensile strength (σ_c, fj_ten), the bond breaks. Program users can specify the tensile strength directly in the console pane displayed on the program's user interface. At the same time, the shear stress of an element is more than bond shear strength ($\tau_c^{(e)}$), the bond breaks due to shear stress. However, because the shear strength depends on the magnitude of normal stress acting on the element (shear strength increases when the contact interface experiences high normal stress), program users cannot specify the shear strength value. Instead, PFC calculate the shear strength that follows the Coulomb limit, shown in Equation 2.22. Therefore, we can specify only two bond parameters: bond cohesion (c, fj_coh) and friction angle (ϕ, fj_fa).

Unbonded condition: $$\tau_c^{(e)} = c - \sigma^{(e)} tan\phi \quad (2.22)$$

The element turns from bonded to unbonded when the bond breaks due to tensile stress or shear stress. If the element breaks due to tensile stress, there is no tension force holding the two balls together. Whereas, if the element breaks due to shear stress, the contact interface still has a frictional force that acts along a tangential direction, and the shear strength of the frictional surface is

$$\tau_c^{(e)} = -\mu\sigma^{(e)} \quad (2.23)$$

Where μ is the friction coefficient (fj_fric).

Chapter 3: Parametric Study and Generation of Flat-Joint Models

Because the flat-joint bond properties (micro properties) assigned in the model do not correspond to the material properties (macro properties), and there is no precise equation for calibrating these micro and macro properties. While some researchers have investigated the statistical relationship between these properties, the model is constrained by ball radius. If the scale of the simulation is large (large model with many small-radius balls), the computer may not be capable of handling the large dataset. However, if they decide to increase the size of balls, they cannot use those given equations from previous research studies.

Therefore, program users may be required to calibrate by changing each micro parameter to match a desired macro property iteratively. The process of micro parameter iterative process takes multiple times to achieve the desired material property. Moreover, each input parameter could alter more than one macro property. Consequently, performing numerous iterations is a time-consuming and ineffective method. Due to the large number of balls generated by some simulations, computer processing may take hours; additionally, an intricate simulated material containing clumps and clusters requires additional processing time, possibly even days. So, a practical approach is necessary to minimize the calibration time process. This study emphasizes the importance and impact of editable micro properties on the macro properties of the flat-joint contact model by demonstrating an easy-to-use procedure for creating material for flat-joint models in the PFC2D. This procedure results in fewer calibration errors and have a less iterative process.

3.1 Methodology

As described in Chapter 2 that a bonded element's behavior is linearly elastic. An unbonded element is linearly elastic and frictional, with slip accommodated by imposing a Coulomb limit on the shear force, Equation 2.20-2.23. There are four editable that could affect the bond tensile strength and bond shear strength.

1. Effective modulus (E*)
2. Tensile strength (σ_c)
3. Cohesion (c)
4. Normal-to-shear stiffness ratio (κ*)

The parametric study of these five microparameters is conducted out through uniaxial compressive and direct tension simulations. This parametric study varies one micro parameter, while the remaining four remain constant. Effective modulus (E*, emod) assumes four different values. Tensile strength (σ_c, fj_ten), Cohesion (c, fj_coh), and Normal-to-shear stiffness ratio (κ*, kratio) each have three different values as shown in Table 3.1. As a result, this study contains 108 different combinations of simulated materials.

Table 3.1 Value of the assigned microparameters.

Flat-Joint parameters	**Value**	**Unit**
Effective modulus	10, 20, 30, 40	GPa
Normal-to-shear stiffness ratio	1, 2, 3	
Cohesion	5, 10, 15	MPa
Tensile strength	2, 4, 6	MPa

However, other input parameters, friction coefficient (μ) and friction angle (ϕ), are not included in this study. The sample's ball distribution is randomly arranged and has a uniformly distributed radius from 0.3 to 0.4 millimeters, with a single density of 2400 kilograms per cubic meter, as shown in Table 3.2.

Table 3.2 Material geometry, ball properties, and fixed bond parameters.

Material geometry	**Value**	**Unit**
width	5.00	cm
height	10.00	cm
Ball		
Radius (uniformly distributed)	0.30-0.40	mm
density	2400.00	kg/m^3
Contact properties		
gap	0.20	mm
friction coefficient	0.50	

After generating the bonded material, the ball radius is uniformly distributed between 0.3 and 0.4 millimeters, resulting in 11606 balls with a width of 5 centimeters and a height of 10 centimeters. Figure 3.1 illustrates the distribution of balls in the simulated sample. The color represents the radius of the ball; the blue balls are 0.3 millimeters in radius, while the red balls are 0.4 millimeters in radius.

3.1.1 Uniaxial compressive simulations

During the uniaxial compressive simulations, the top wall and bottom wall (shown in black lines in Figure 3.1) have a velocity of 5 millimeters per second in the opposite direction, compressing the simulated materials. The top wall has a vector of movement vertically downward, while the bottom wall has a vector of movement vertically upward. Although a wall velocity of 5 millimeters per second appears extremely fast, in reality, it does not affect the simulation result as long as the model remains in quasi-static equilibrium. A maximum step strain rate of 1.1×10^{-8} $step^{-1}$ is appropriate, according to Zhang and Wong (2014)

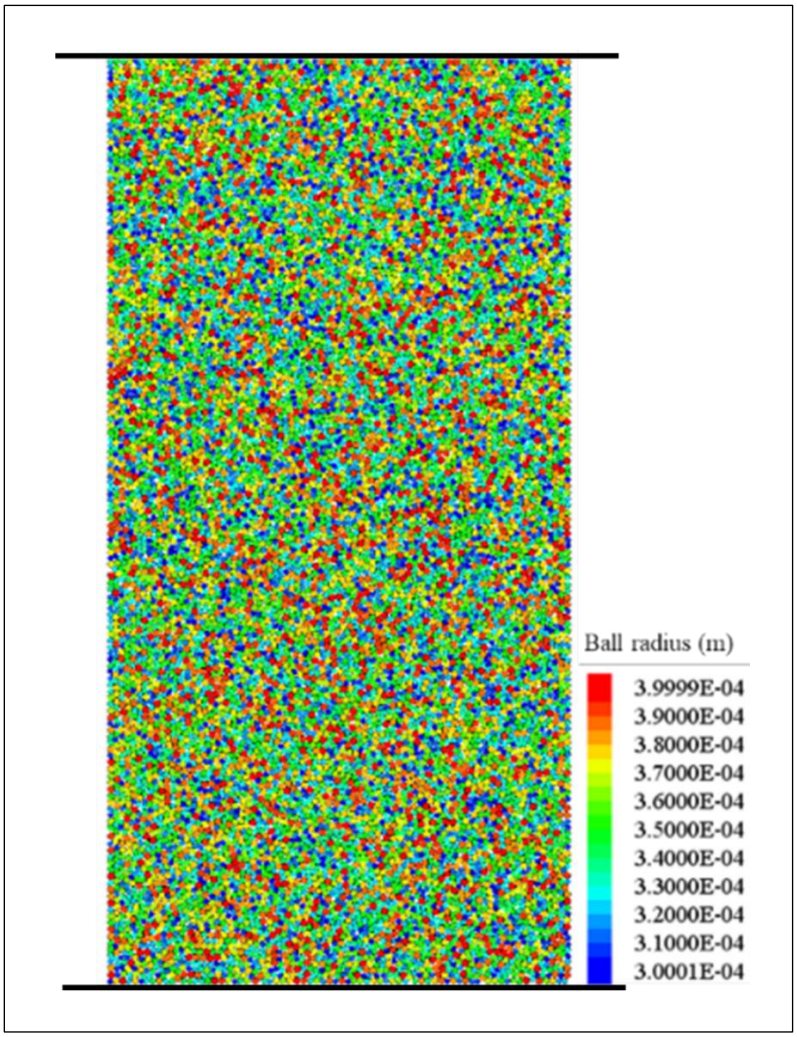

Figure 3.1 ball size distribution in the sample.

When two walls compress the simulated material, the material reacts the force back to the walls, as shown in Figure 3.2. Balls attached at the top wall provide the forces vertically upward, while balls attached at the bottom wall provide the forces vertically downward. The color of the arrow represents the force's magnitude in Newtons. When the walls continue to compress, the force exerted by each ball on them changes and updates continuously.

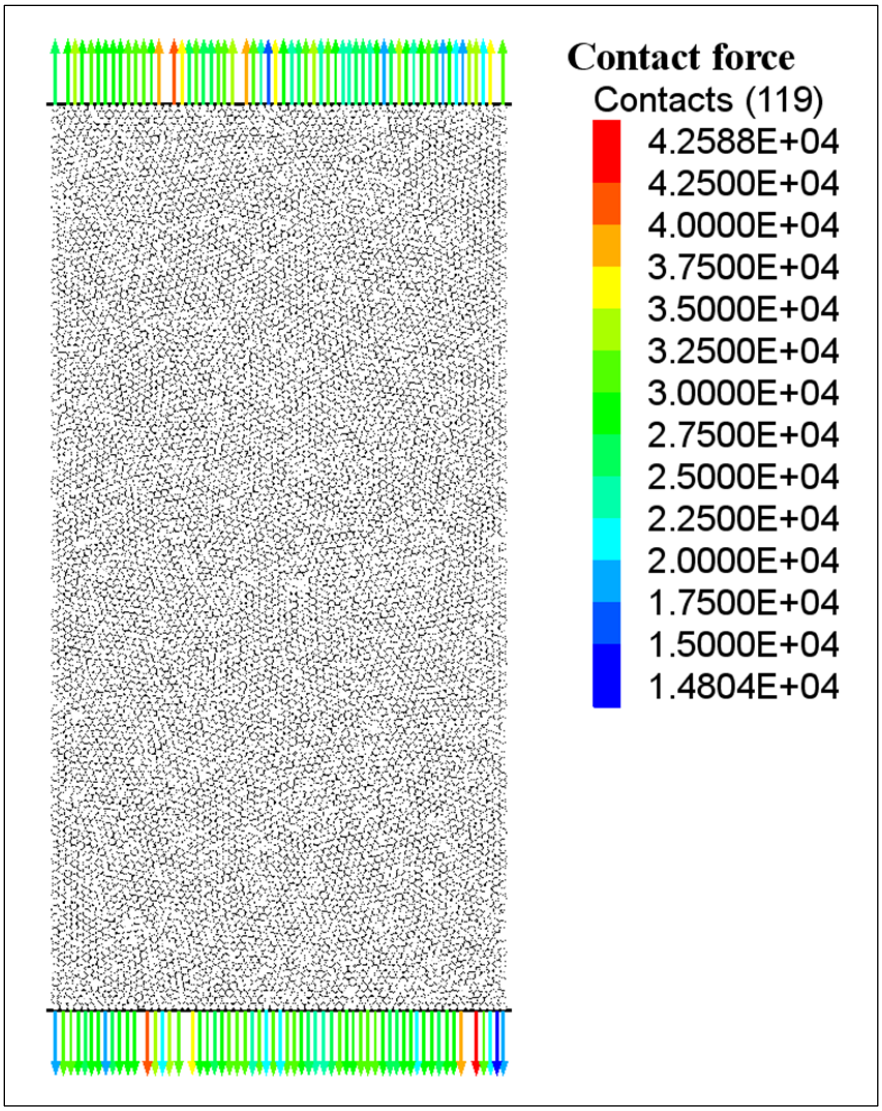

Figure 3.2 Force vectors acting to walls during the compressive simulation.

Forces acting on the top and bottom walls of the uniaxial compressive simulations were recorded. The total force applied to the sample is equal to half of the summation of the contact forces acting on the top and bottom walls as calculated with the FISH function "wall.force.contact". According to this study on the 2D domain, the sample's cross-section areas are the sample's width because $\hat{k}$ vector is a depth of unit thickness. Therefore, the stress calculation of the uniaxial compressive simulation is

$$\sigma = \frac{1}{2} \times \frac{(\text{force}_{\text{top wall}} + \text{force}_{\text{bottom wall}})}{\text{sample width}} \tag{3.1}$$

The axial strain in the uniaxial compressive simulation can be monitored from balls at the top and bottom walls, divided by the sample's initial height.

$$\varepsilon = \frac{\Delta L_{\text{top wall displacement}}}{\text{sample height}} + \frac{\Delta L_{\text{bottom wall displacement}}}{\text{sample height}} \tag{3.2}$$

As a result of the top and bottom moving simultaneously, the top and bottom walls have the same displacement. Therefore, the axial strain in the uniaxial compressive simulation is

$$\varepsilon = 2 \times \frac{\Delta L_{\text{wall displacement}}}{\text{sample height}} \tag{3.3}$$

Each compressive simulation is halted when the applied stress reaches the compressive strength and drops to 90% of its strength.

3.1.2 Direct tension simulations

Unlike the compressive simulations, the direct tension simulations do not have top and bottom walls. However, these simulations design balls at the top and the bottom to move in opposite directions. So, balls at the topmost are moving up, whereas balls at the bottommost move down at a velocity of 5 millimeters per second, creating simulated material experienced in tension. This velocity remains the model in static equilibrium. However, because the direct tension simulations do not have walls, we cannot record forces acting on walls the same way we do for uniaxial compressive simulations. Christoffersen (1981), on the other hand, introduced the stress measurement by defining an interesting region in the sample (typically a circle in the center of the sample), shown in Figure 3.3, and recording the total force in this region using the following equation:

$$\sigma = -\frac{1}{\mathrm{V}} \sum_{N_c} F^{(c)} \otimes L^{(c)} \tag{3.4}$$

where N_c is the number of contacts in the measurement region, $F^{(c)}$ is contact force, $L^{(c)}$ is the branch vector joining the centroids of the two bodies in contact, $\otimes$ denotes outer product, and compressive stress is negative by convention.

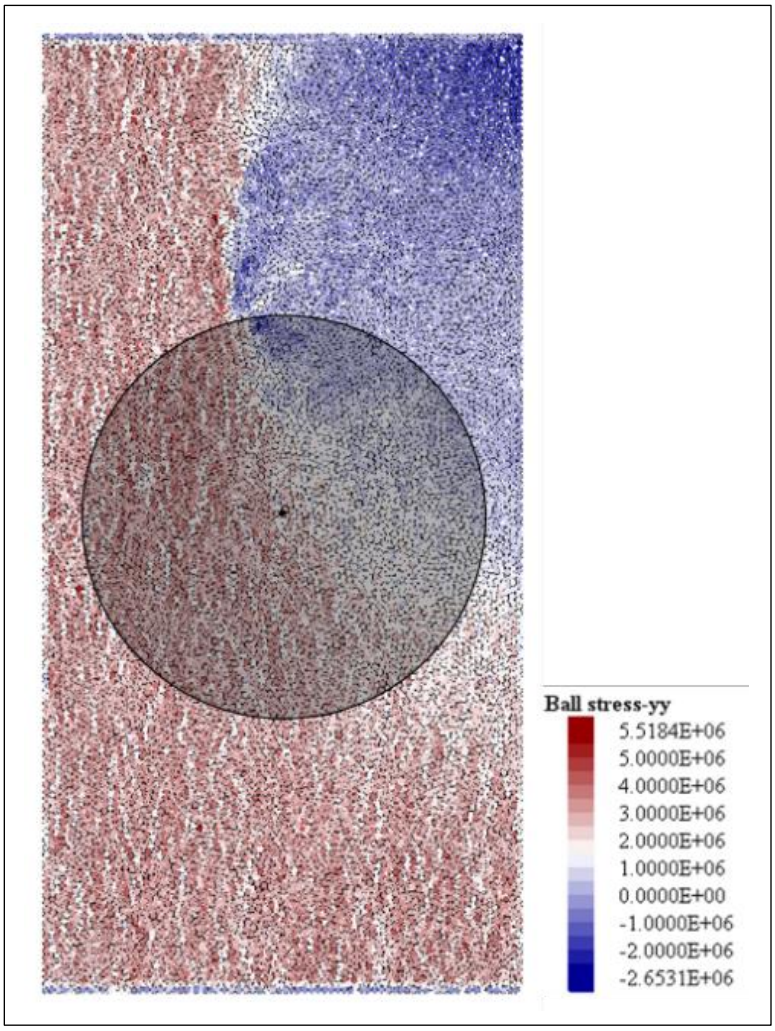

Figure 3.3 Axial stress monitoring using the total force within the interesting area (circular black region).

The axial strain in the direct tension simulation can be monitored using the same method as in the uniaxial compressive stimulation by measuring the displacement of balls at the top and bottom walls. Each direct tension simulation is halted when the applied stress reaches the tensile strength and drops to 90% of its strength.

3.2 Simulation results

Each assigned micro property shows a different result on the macro property. Some parameters slightly affect the compressive strength, tensile strength, and overall strain. On the other hand, some parameters significantly influence the material properties. Appendix A

contains the results of 108 compressive simulations and 108 direct tension simulations, which include calculated simulated material Young's modulus, simulated material compressive strength, simulated material tensile strength, and compressive strength to tensile strength ratio.

3.2.1 Bond effective modulus (emod)

Assigning a bond effective modulus can directly change the material modulus. However, according to all 208 tests, the assigned bond effective modulus values are lower than the macro property modulus. To illustrate, when emod is 20 GPa, the calculated material modulus is 37 GPa. The discrepancy has become more expansive when the value of the effective modulus is high. Figure 3.4 shows the relationship between bond effective modulus (emod) and calculated macro property modulus based on the data from Appendix A. Each line has the same Normal-to-shear stiffness ratio, cohesion, and tensile strength properties.

Figure 4(B) shows the data from simulation numbers 17-20 (black), 53-56 (red), and 89-92 (green). All simulations have the same normal-to-shear stiffness ratio (kratio) of 2.0 and flat-joint tensile strength of 4.0 MPa. The only flat-joint cohesion (fj_coh) values change. We can observe that these three lines are stacked together, which means varying fj_coh does not alter macro property modulus.

Whereas, Figure 4(C) shows the data from simulation numbers 13-16 (red), 17-20 (black), and 21-24 (green). All simulations have the same flat-joint tensile strength of 4.0 MPa and flat-joint cohesion of 5 MPa. The only normal-to-shear stiffness ratio values change. From the observation, all three lines have different macro property modulus. Therefore, it can be concluded that the normal-to-shear stiffness ratio has a significant effect on modulus.

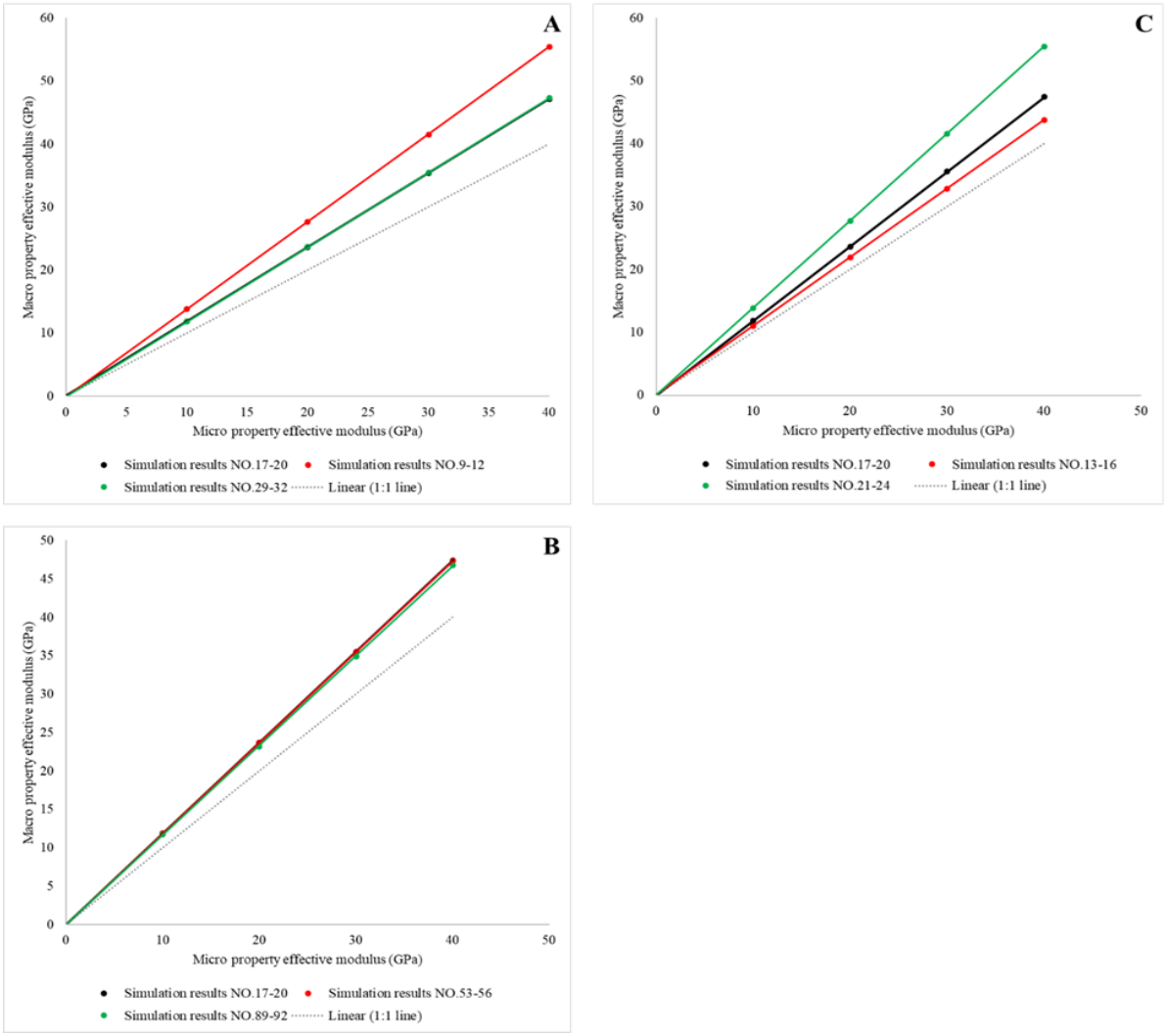

Figure 3.4 The response of macro property effective modulus due to varying bond effective modulus (emod).

The consequence of compressive strength due to the bond's effective modulus is low. Figure 3.5(A-E) shows that varying the micro property effective modulus of 10, 20, 30, and 40 GPa slightly affects the compressive strength. Furthermore, the bond's effective modulus significantly changes the axial strain. Therefore, increasing the bond's effective modulus can increase material axial strain.

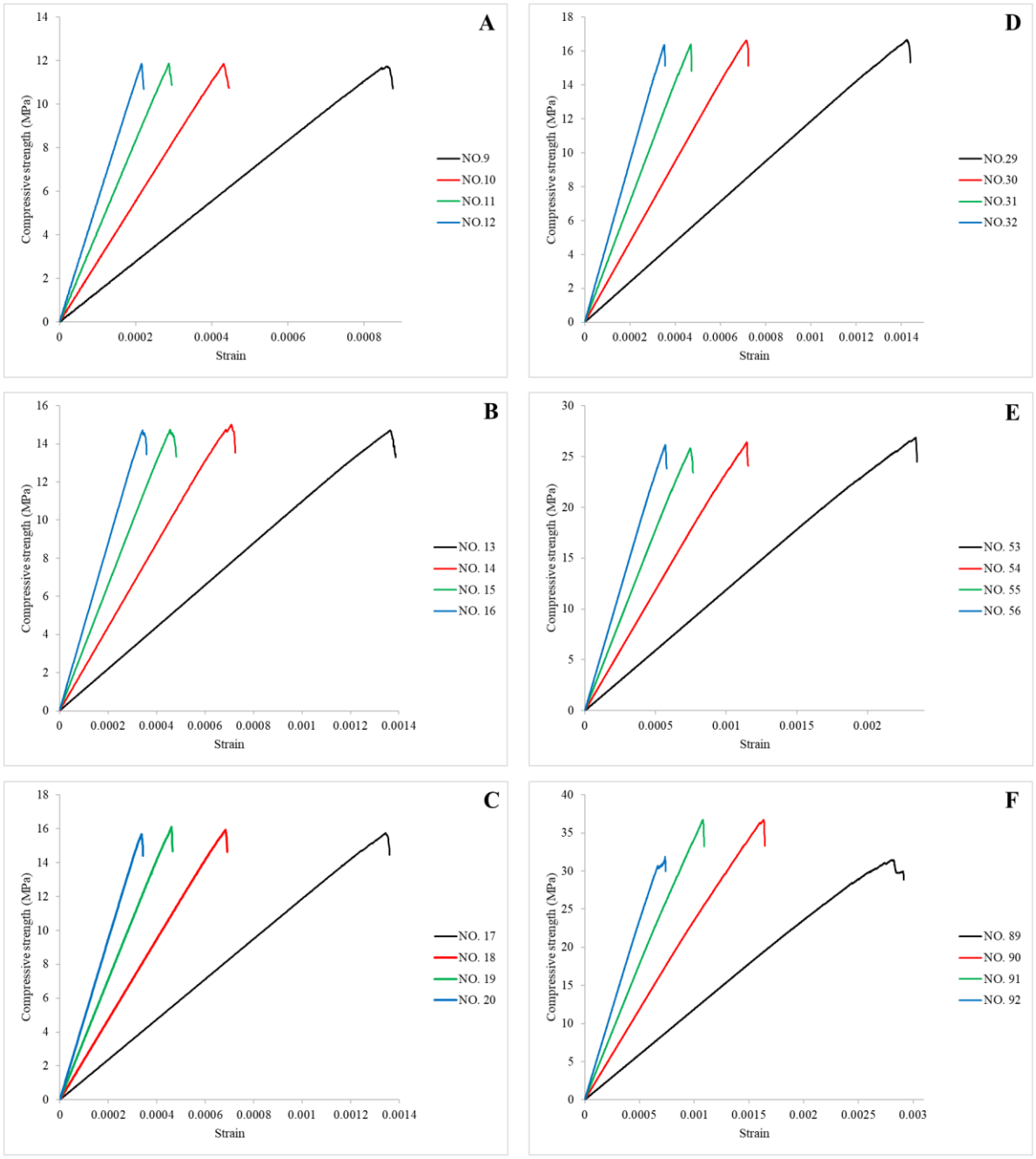

Figure 3.5 Stress-strain curves, A-E graphs show slightly different compressive strength when emod changes.

3.2.2 Normal-to-shear stiffness ratio (kratio)

The normal-to-shear stiffness ratio significantly affects the compressive strength and Poisson's ratio of the material. The increased normal-to-shear stiffness ratio results in a greater Poisson's ratio. However, the impact on tensile strength is negligible (Figure 3.6). As illustrated in Figure 3.6(A, B, C), increasing the normal-to-shear stiffness ratio can either increase or decrease the compressive and tensile strengths of the material. Additionally, the normal to shear stiffness ratio can affect the material modulus and ultimate strain as shown in Figure 3.7.

3.2.3 Bond cohesion (fj_coh)

Bond cohesion (fj_coh) has a significant effect on the compressive strength of macro properties. Increased bond cohesion results in increased compressive strength. As illustrated in Figure 3.8(A), increasing bond cohesion by about 10 MPa from 5 to 15 MPa can double the compressive strength of macro properties with linear proportion. Bond cohesion, on the other hand, does not affect the macro property tensile strength. While bond cohesion increases from 5 to 10 MPa in Figure 3.8(B), the macro property tensile strength remains constant. Thus, if the tensile strength of a synthetic material needs to be adjusted, changing the bond cohesion value does not affect the macro property tensile strength. In comparison, it has a significant effect on compressive strength.

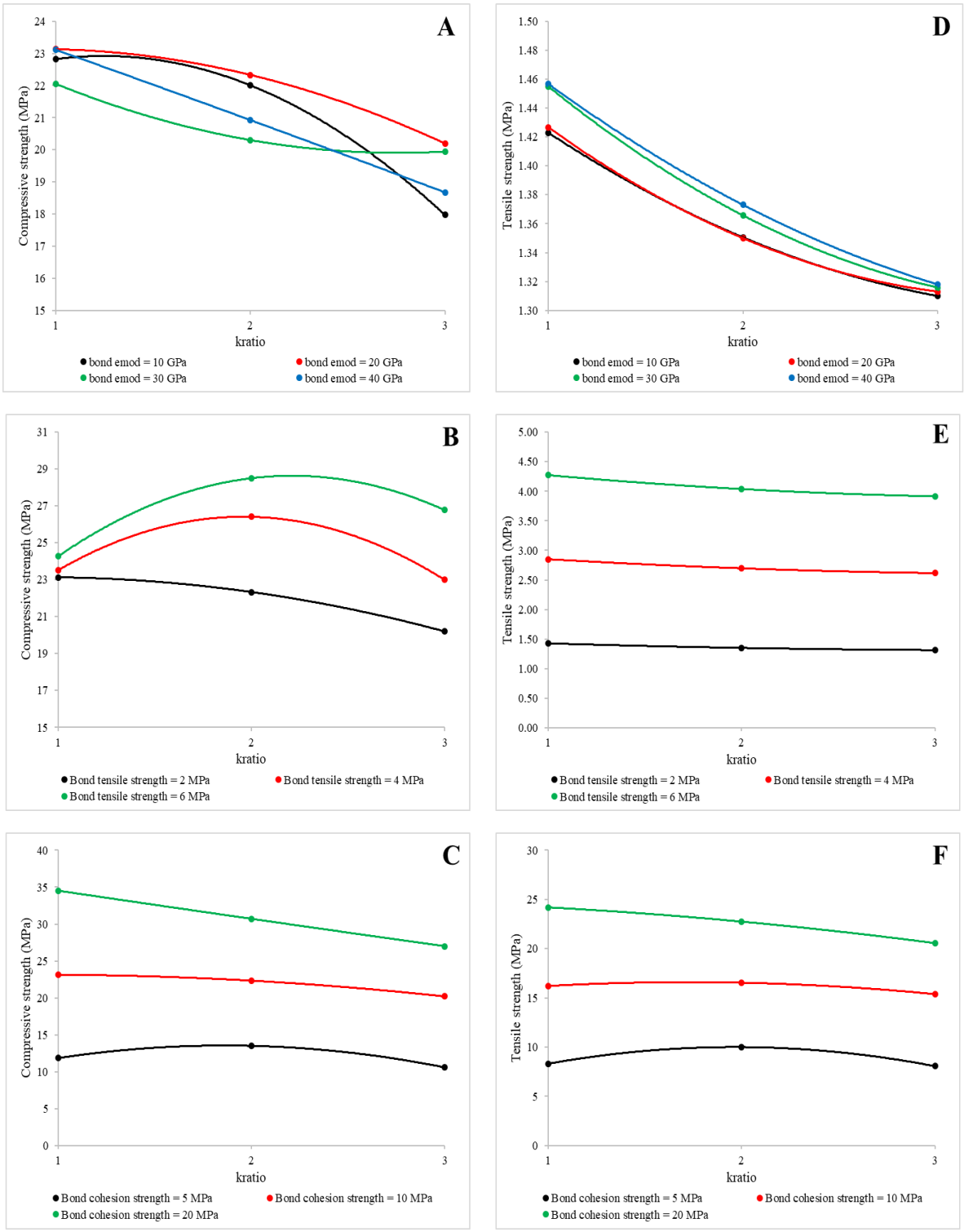

Figure 3.6 Compressive strength and tensile strength of the synthetic materials when kratio changes.

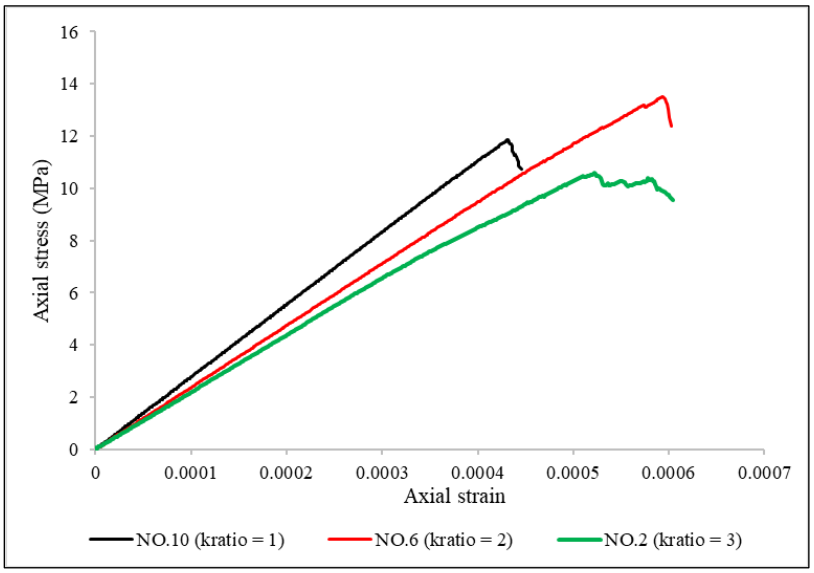

Figure 3.7 Stress-strain curves of 3 uniaxial compressive simulations. According to test NO. 2, 6, and 10.

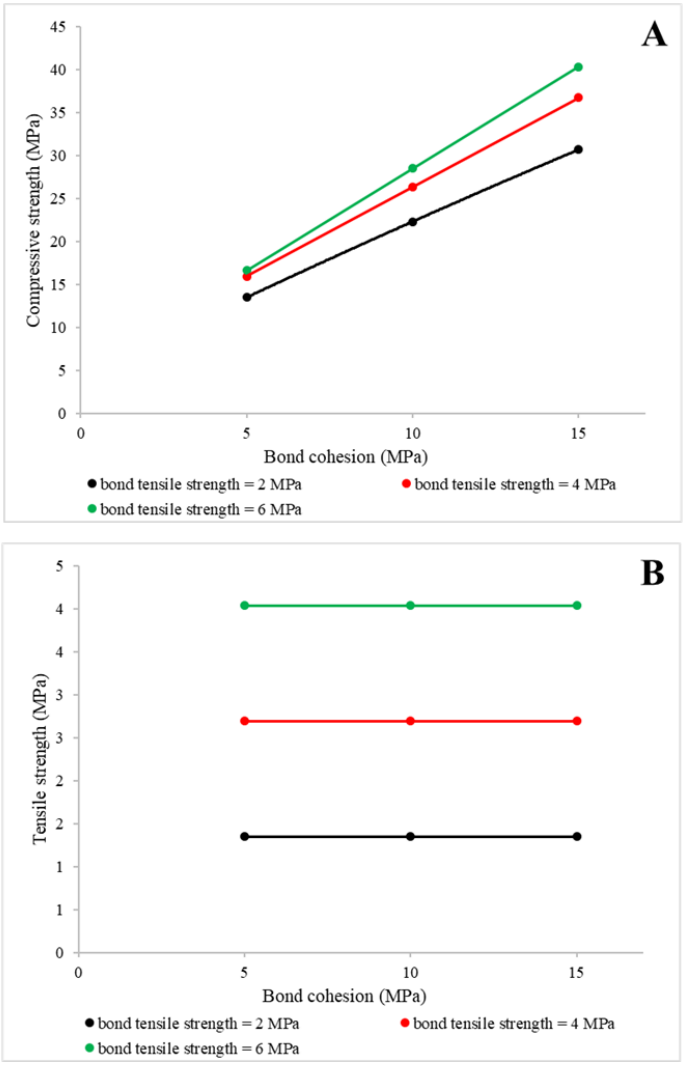

Figure 3.8 Stress-strain curves of the uniaxial compressive simulations (A) and material tensile strength vs. bond cohesion from the direct tension simulations (B).

3.2.4 Tensile strength (fj_ten)

As illustrated in Figure 3.9(A), the compressive strength of a macro property depends on the bond tensile strength. As can be seen from the three different trendlines, fj_coh 5, 10, and 15 MPa have a different degree of slope and are not linear trends. The group of simulated materials with bond cohesion of 5 MPa has a slight change in compressive strength when bond tensile strength increases. In contrast, the group with a bond cohesion of 15 MPa has a more significant effect on compressive strength change. Bond tensile strength (fj_ten) has a significant effect on both the tensile and compressive properties. As illustrated in Figure 3.9(B), increasing bond tensile strength by approximately 4 MPa from 2 to 6 MPa can linearly increase macro property tensile strength by approximately 3 MPa. Additionally, as illustrated in Figure 3.9(B), the data points and trendlines for various bond cohesions overlap.

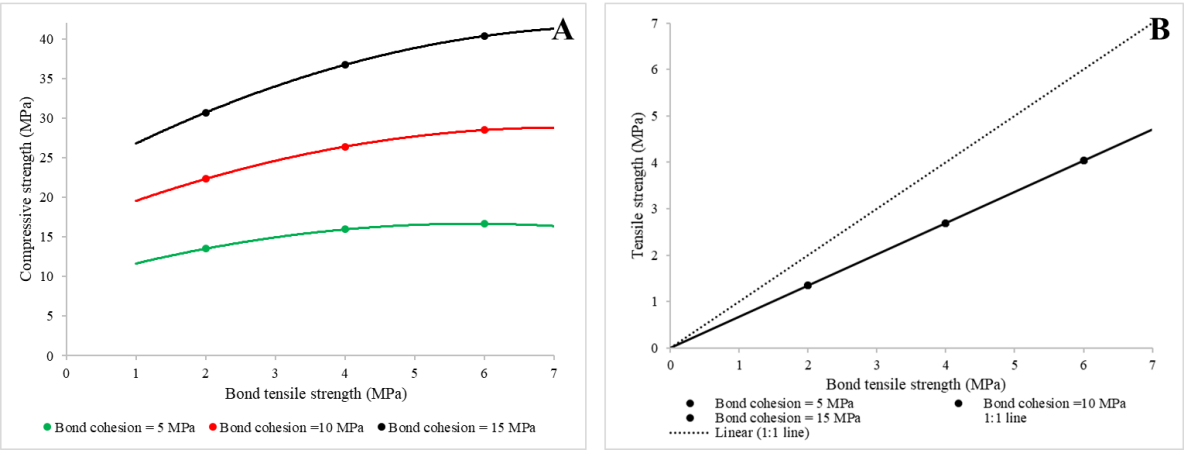

Figure 3.9 Relationship between material compressive strength and bond tensile strength (A), and material tensile strength and bond tensile strength (B).

3.3 Simulations and material generation observations

According to 108 uniaxial compressive simulations and 108 direct tension simulations, the data reveals five input bond parameters including Effective modulus (E*, emod), Tensile strength (σ_c, fj_ten), Cohesion (c, fj_coh), and Normal-to-shear stiffness ratio (κ*, kratio) affect the simulated material differently. Changing a single bond parameter can have a multiplicity of effects on the material's properties. As a result, increasing or decreasing a bond parameter may cause a simulated material to become miscalibrated for other material properties. The observations are summarized in the following nine lists;

1. Changing Effective modulus (emod) can alter the material compressive strength.
2. Effective modulus (emod) is not equal to the material's Young's modulus.
3. Normal-to-shear stiffness ratio (kratio) directly affects Poisson's ratio.
4. Normal-to-shear stiffness ratio (kratio) increases/decreases the material’s compressive/tensile strength.
5. Normal-to-shear stiffness ratio (kratio) changes the material's Young's modulus.
6. Bond cohesion (fj_coh) increases the material's compressive strength proportionally.
7. Bond cohesion (fj_coh) does not impact the material's tensile strength.
8. Bond tensile strength (fj_ten) affects the material's compressive strength.
9. Bond tensile strength (fj_ten) is not equal to the material's tensile strength.

The procedure for generating a simulated material in the PFC2D depends on the mentioned nine observations. These observations are needed to reorder because each latter parameter's calibration affects previously calibrated parameters. Therefore, the suggestion of the calibrating steps are:

1. Normal-to-shear stiffness ratio (kratio)
2. Bond tensile strength
3. Effective modulus (emod)
4. Bond cohesion (fj_coh)

The following steps suggest calibrating simulated materials in the PFC2D to match the rock properties obtained from laboratory experiments and describe which properties should be focused on during each calibration step. Additionally, Figure 3.10 illustrates the material generation process as a flowchart.

1. Identifying the laboratory-derived material properties that are simulated in the PFC. The compressive strength, tensile strength, modulus of elasticity, and, if possible, Poisson's ratio of the material must all be recorded. Each test should have an identical sample size to avoid errors caused by sample geometry. Compressive or tensile stress versus strain data was used to calculate the macro properties mentioned previously.

2. After finishing laboratory tests of the samples, the next step is to work on the PFC program. Unbonded material is created, which has the same size as the laboratory specimen. Because this study works on 2-Dimensional simulation, but the laboratory specimen is on three dimensions. The sample width in the PFC2D model corresponds to the cylindrical specimen's diameter, and the sample height corresponds to the height of the cylindrical specimen. The balls generated should not be excessively large but relatively small enough to maximize the computer's processing capacity. Ball density and porosity should be comparable to those of the laboratory specimen.

3. The built-in flat-joint contact model can be assigned the sample. To obtain a Poisson's ratio of 0.2, the normal-to-shear stiffness ratio (fj_kratio) should be approximately 2.5. This value may be altered if Poisson's ratio varies. If the friction angle from a laboratory test is known, the friction angle (fj_fa) can be approximated. This micro property friction angle also influences the mode of failure and degree of fracture of the material. The initial assignment micro properties are the flat-joint tensile strength (fj_ten) and

flat-joint effective modulus (fj_emod), derived from laboratory results to simulate the first iteration.

4. Conduct the uniaxial compressive test; both the top and bottom walls should have a maximum step strain rate of 1.1×10^{-8} $step^{-1}$, indicating that the model is in quasi-static equilibrium. To verify that the model is in quasi-static equilibrium, we can look at the stress-strain curve and observe that the data point should be linear up to the peak stress. If the stress-strain curve oscillates in the early elastic range, the loading rate is too high, and the velocity of the walls should be decreased (Xiao-Ping Zhang and Louis Ngai Yuen Wong, 2014). Next, calculate the Poisson's ratio of the material after the first simulation is complete. If the normal-to-shear stiffness ratio (fj_kratio) does not meet the target, increase or decrease it in the next iteration.

5. When the synthetic material has attained the desired Poisson ratio, conduct a tension test to determine the sample's tensile strength. The micro parameters used in this step remain the same as in step 4. Thus, iteration 1 refers to the properties of this bond. Next, calculate the material's tensile strength.

6. If the calculated material's tensile strength does not match the laboratory tensile strength, perform additional iterations by varying the flat-joint tensile strength (fj_ten) until the calculated material's tensile strength matches the laboratory tensile strength. Other micro properties remain constant.

7. The process of tensile strength calibration is complete when the sample reaches the specified tensile strength. The next step is to calibrate the effective modulus value. First, conduct a uniaxial compressive test to obtain a stress-strain curve from which the effective modulus can be calculated. Suppose the effective modulus of the macro property is not identical to the effective modulus of the laboratory. In that case, this can be accomplished by iteratively varying the effective modulus of the micro property (emod). Iterate until the simulation material's effective modulus matches the value obtained in the laboratory. Notably, the tensile strength of the simulation remains constant or has changed insignificantly.

8. When the simulated material has the desired tensile strength and modulus of elasticity, the compressive strength can be the final property to be calibrated and adjust this property by modifying the flat-joint cohesion (fj_coh). It has an indirect effect on the compressive strength of the material. This step involves performing a uniaxial compressive test, and adjust the simulation's uniaxial compressive strength until it approaches the desired laboratory compressive strength.

9. When the model compressive strength meets the desired value. Verify the model's tensile strength and modulus. It may vary slightly. If they are within an acceptable range and the failure mode is acceptable, the procedure for material genesis is completed.

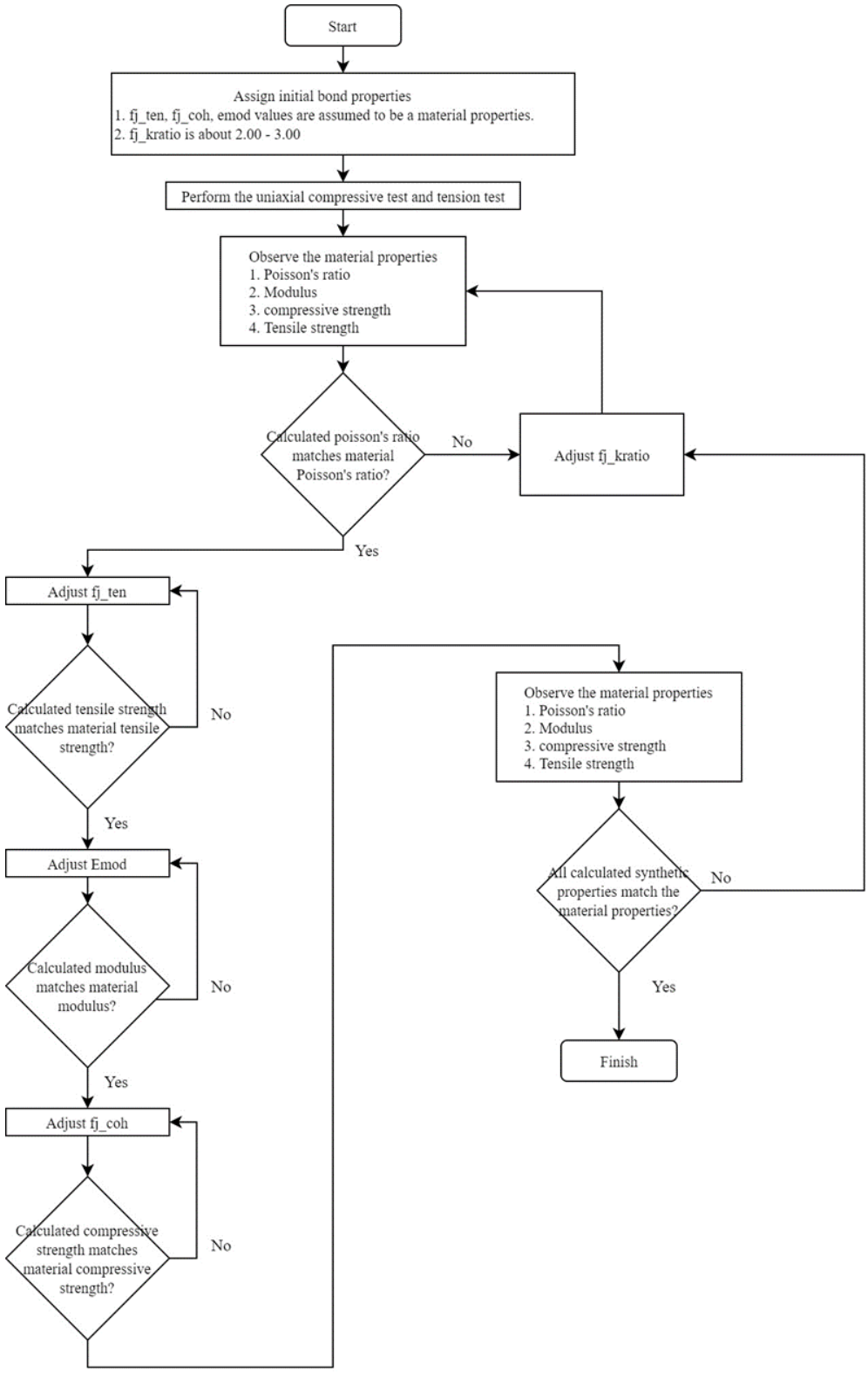

Figure 3.10 Procedure for the generation of material for flat-joint models in PFC6.0.

3.4 Validation of the Procedure

The provided material genesis procedure has 9 steps and needs to be validated. This study requires the uniaxial compressive tests and tension tests. These tests are used to determine the material's response to applied loads, including the compressive strength, the tensile strength, Young's modulus, and the mode of failure. Validation materials consist of a mixture of sand and cement. Natural rocks are not used to validate this procedure because they are heterogeneous and may exhibit erratic microstructures, which complicates validation.

Five samples are prepared for testing, three for the uniaxial compressive tests, and two for the tension tests. The sample mixture proportion by volume of concrete mix of cement: sand is 1:1.5 to analyze for the homogenous material study. The estimated weight of cement and sand per cubic meter is 904 and 1507 kilograms. The wet mixtures are filled into 10-by-20-centimeter concrete cylinder molds and are cured for 28 days to let the moisture leaves the samples. ASTM C 39/ C 39M (standard test method for compressive strength of cylindrical concrete sample) is the standard for the uniaxial compressive tests. The applied loading rate is 0.25±0.05 MPa per second.

In contrast, ASTM C 496/C 496M (standard test method for splitting tensile strength of cylindrical concrete specimens) is the standard test of the tension tests. The applied loading rate was within 0.7 to 1.4 MPa per minute. The values of compressive strength, tensile strength, stress-strain relationship, and failure mode are recorded. These values are used for assigning the bond properties in the PFC simulations because the compressive strength, tensile strength, and Young's modulus of these samples are the initial micro properties assigned in the material genesis procedure.

3.4.1 Sample testing

3.4.1.1 The uniaxial compressive tests

Table 3.3 provides the physical properties of three samples, weight, density, and geometry, and Figure 3.11 shows an example of a cylindrical sample. The compressive strengths of the three samples are 27.95, 30.27, and 29.50 MPa. The average compressive strength is 29.24

MPa. Figure 3.12 shows the relationship between compressive stress and the axial strain. According to the result of the tests, the average Young's modulus of the samples is 9.3 GPa. After the compressive stress reaches the ultimate compressive stress at 30 MPa, the stress decreases substantially to 5 MPa and remains constant until tests stopped.

Table 3.3 Sample properties for the uniaxial compressive tests.

Properties	**Sample NO.1**	**Sample NO.2**	**Sample NO.3**
Diameter (mm)	101.85	101.90	101.44
Height (mm)	200.67	101.92	201.83
Calculated cross-section area (m^2)	0.00815	0.00815	0.00808
Volume (m^3)	0.00164	0.00165	0.00163
Mass (kg)	3.652	3.685	3.696
Calculated density (kg/m^3)	2233.80	2236.60	2266.00

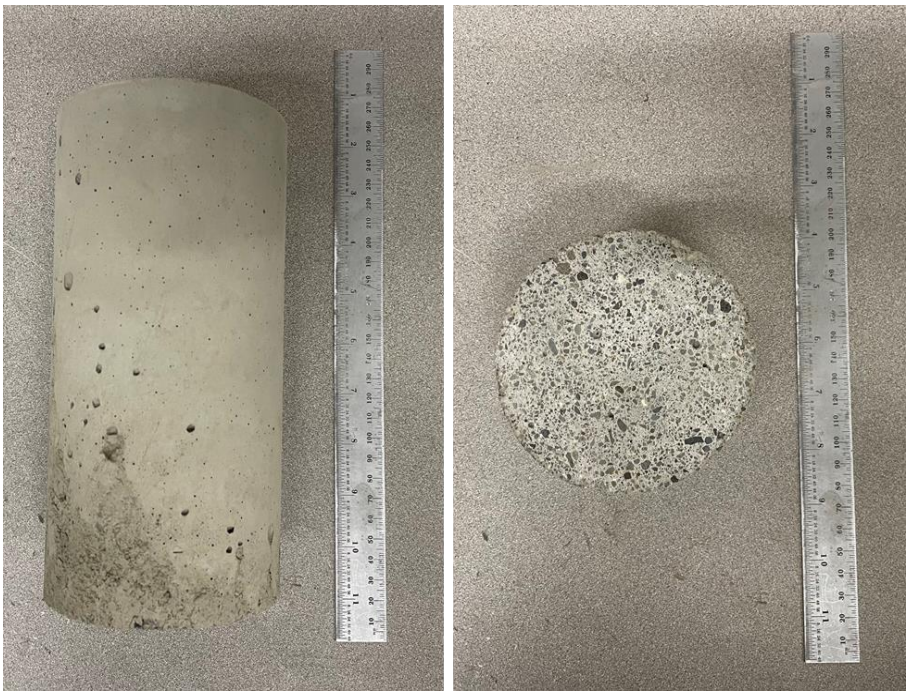

Figure 3.11 Cylindrical sample for laboratory tests.

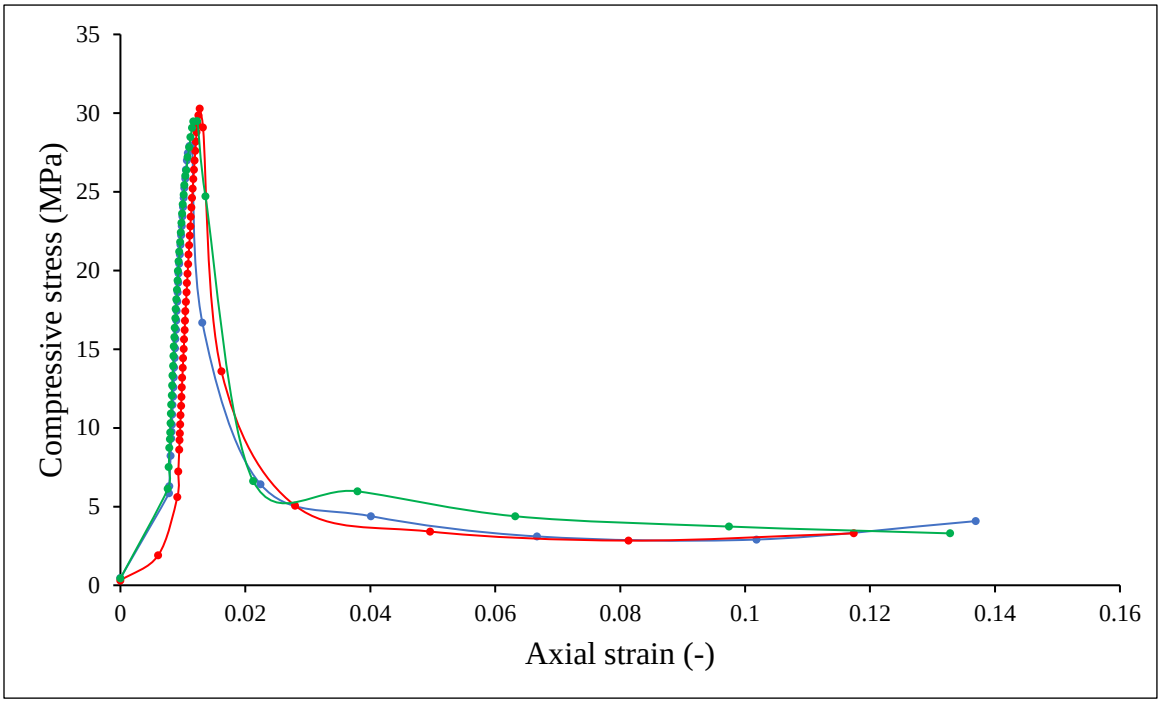

Figure 3.12 Strain-strain curves of the uniaxial compressive tests.

The post-failure pattern of three samples is columnar vertical cracking through both ends, no well-formed cones, according to 6 types of well-defined pattern in ASTM C39/C 39M. This fracture pattern orientates parallel to the axial axis or perpendicular to the force without diagonal fracture (Figure 3.13).

3.4.1.2 The tension tests

The stress-strain curves are monitored during the tension tests. The tensile strengths of the two samples are 3.51 and 3.32 MPa. The average tensile strength is 3.41 MPa. Figure 3.14 shows the relationship between tensile stress and strain.

Figure 3.13 The sample failure after the compressive test.

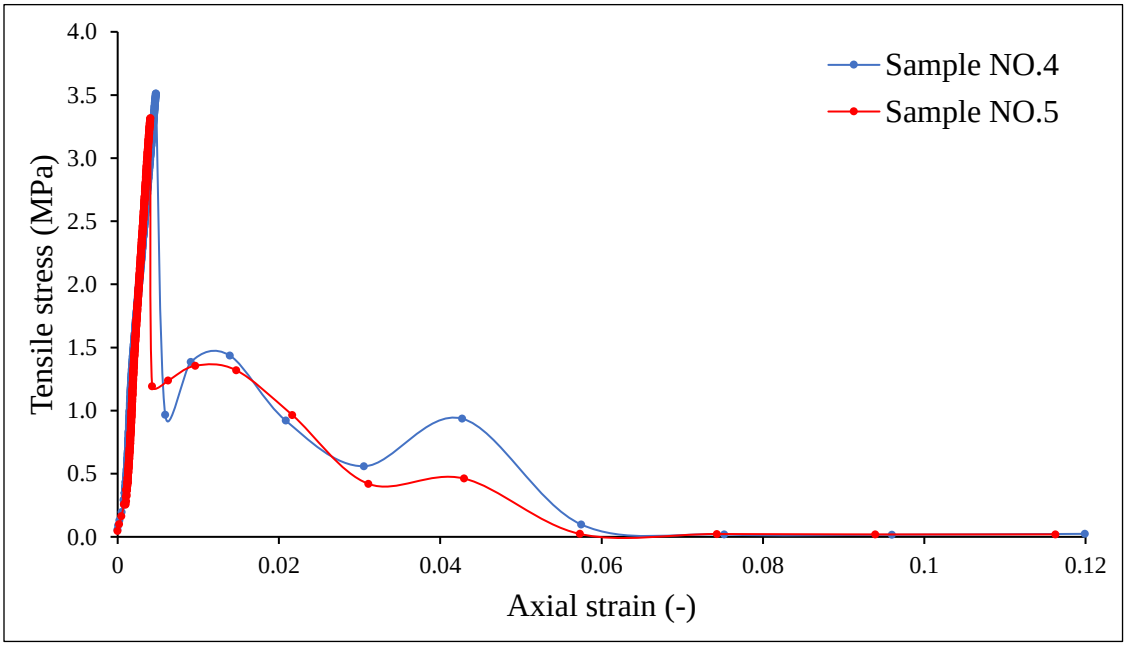

Figure 3.14 Strain-strain curve of the tension tests.

3.4.2 Calibration process in PFC2D

To validate the procedure for the generation of material in PFC2D, the following steps were carried out. Firstly, the uniform distribution of balls with radius ranges between 0.7 to 0.9 millimeters is generated in the 10 centimeters width and 20 height box (Figure 3.15 (A)). Secondly, the ball's density is set to 2245 kilograms per cubic meter. After entirely distributing balls in the box, the bond properties are assigned (Figure 3.15 (B)). The values of bond properties in the first iteration are 9.31 GPa of bond effective modulus (emod), 3.41 MPa of the bond tensile strength (fj_ten), and 11.4 MPa of bond cohesion (fj_coh). According to the procedure provided, the property needed to calibrate is the material tensile strength. Therefore, the first simulation is the tension simulation.

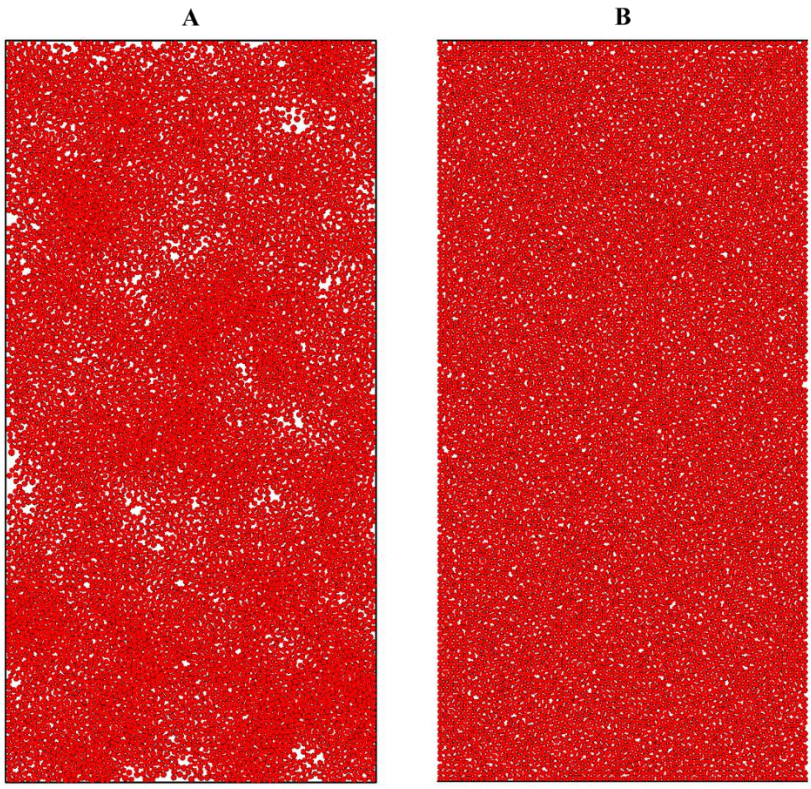

Figure 3.15 Ball distribution after assigning balls to the model (A) and after the model is static (B).

After performing the first iteration of the tension simulation, the tensile strength of the simulated material is 2.57 MPa. In comparison to laboratory measurements, this iteration has a 24.53 percent error. Due to the significant discrepancy between the simulation and laboratory experiment values, additional calibration iterations of tensile strength are required to minimize the error between simulation and laboratory experiments. In addition, the bond tensile strength value should be increased; because the tensile strength of the simulated material is significantly less than the laboratory value. According to this calibration, four iterations achieve the calibration process to match the laboratory tensile strength at 3.41 MPa (Table 3.4).

Once the tensile strength of the simulation matches the laboratory tensile strength, then the uniaxial compressive simulations on the PFC are used to calibrate the material's Young's modulus. Iteration 4 has a modulus of 10.7 GPa with a 14.56% error. Young's modulus of the simulated material is high, implying that the effective modulus (emod) must be reduced. As a result, three iterations calibrate the simulated material's tensile strength to match the laboratory tensile strength from iteration 4 to iteration 7, resulting in an error of 0.71 percent.

After calibrating the material tensile strength and Young's modulus, the next step is adjusting bond cohesion (fj_coh) to match the material compressive strength. At iteration seven, 11.4 MPa flat-joint cohesion results in a material compressive strength of 23.4 MPa; the percentage error between simulated and laboratory compressive strengths is approximately 19.88%. Thus, bond cohesion has to be increased in order to achieve the desired compressive strength. Iteration nine is the last iteration when the simulated material's compressive strength matches the material compressive strength obtained from a laboratory experiment.

Tensile strength, modulus, and compressive stress errors between simulation and laboratory experiments are 0.16%, 0.12%, and 0.04%. As illustrated in Figure 3.16, all three properties' errors converge to 0%. The latest iteration bond properties are 8.1 GPa fj_emod, 4.52 MPa fj_ten, and 14.6 MPa fj_coh (Table 3.4). The compressive stress and strain curve of iteration 9 (Figure 3.17) shows that this specimen has a compressive strength of 29.2 MPa and a modulus of 9.32 GPa, nearly identical to the laboratory samples. Figure 3.18 illustrates the forming of microcracks and fragmentation during the compressive simulation and test. Black lines denote

bond failure, transitioning from the bonded to the unbonded condition, which corresponds to a microcrack, while color denotes fragment.

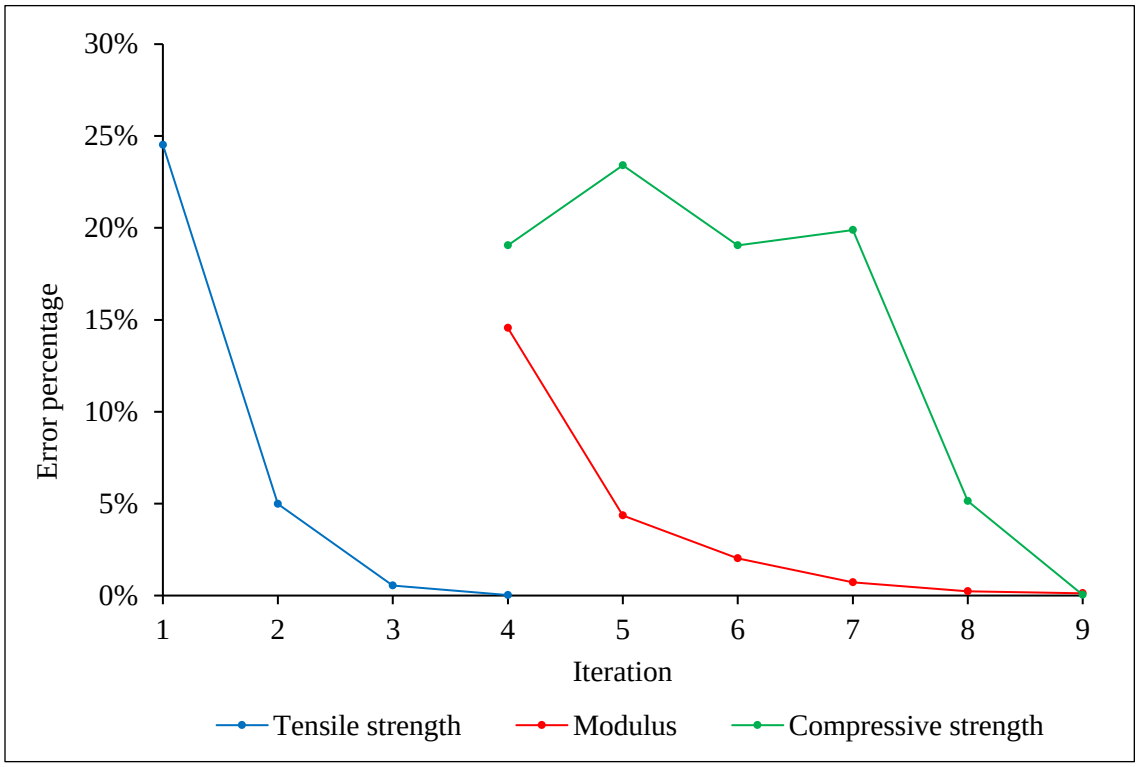

Figure 3.16 Error between PFC simulation and laboratory experiments.

Table 3.4 Bond properties and calculated macro properties of the simulated materials.

Iteration	Input bond properties			Macro properties						
	fj_emod (Pa)	fj_ten (Pa)	fj_coh (Pa)	Tensile strength (Pa)	Modulus (Pa)	Compressive strength (Pa)	Tensile strength error	Modulus error	Compressive strength error	Test type
1	9.31E+09	3.41E+06	1.14E+07	2.57E+06	-	-	24.53%	-	-	Tension test
2	9.31E+09	4.75E+06	1.14E+07	3.58E+06	-	-	4.99%	-	-	
3	9.31E+09	4.50E+06	1.14E+07	3.39E+06	-	-	0.54%	-	-	
4	9.31E+09	4.52E+06	1.14E+07	3.41E+06	1.07E+10	2.37E+07	0.03%	14.56%	19.04%	Tension and Compressive tests
5	8.40E+09	4.52E+06	1.14E+07	-	9.71E+09	2.24E+07	-	4.35%	23.41%	Compressive test
6	7.90E+09	4.52E+06	1.14E+07	-	9.12E+09	2.37E+07	-	2.03%	19.04%	
7	8.10E+09	4.52E+06	1.14E+07	-	9.37E+09	2.34E+07	-	0.71%	19.88%	
8	8.10E+09	4.52E+06	1.40E+07	-	9.33E+09	2.77E+07	-	0.23%	5.14%	
9	8.10E+09	4.52E+06	1.46E+07	3.40E+06	9.32E+09	2.92E+07	0.16%	0.12%	0.04%	Tension and Compressive tests

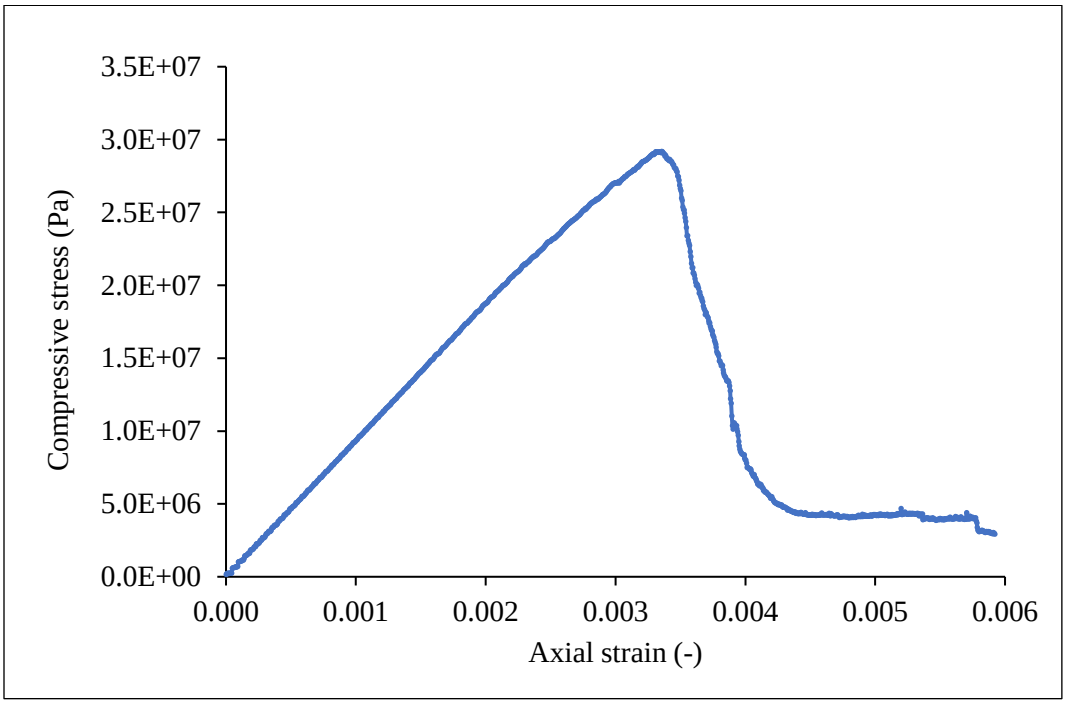

Figure 3.17 Stress-strain curve of iteration 9.

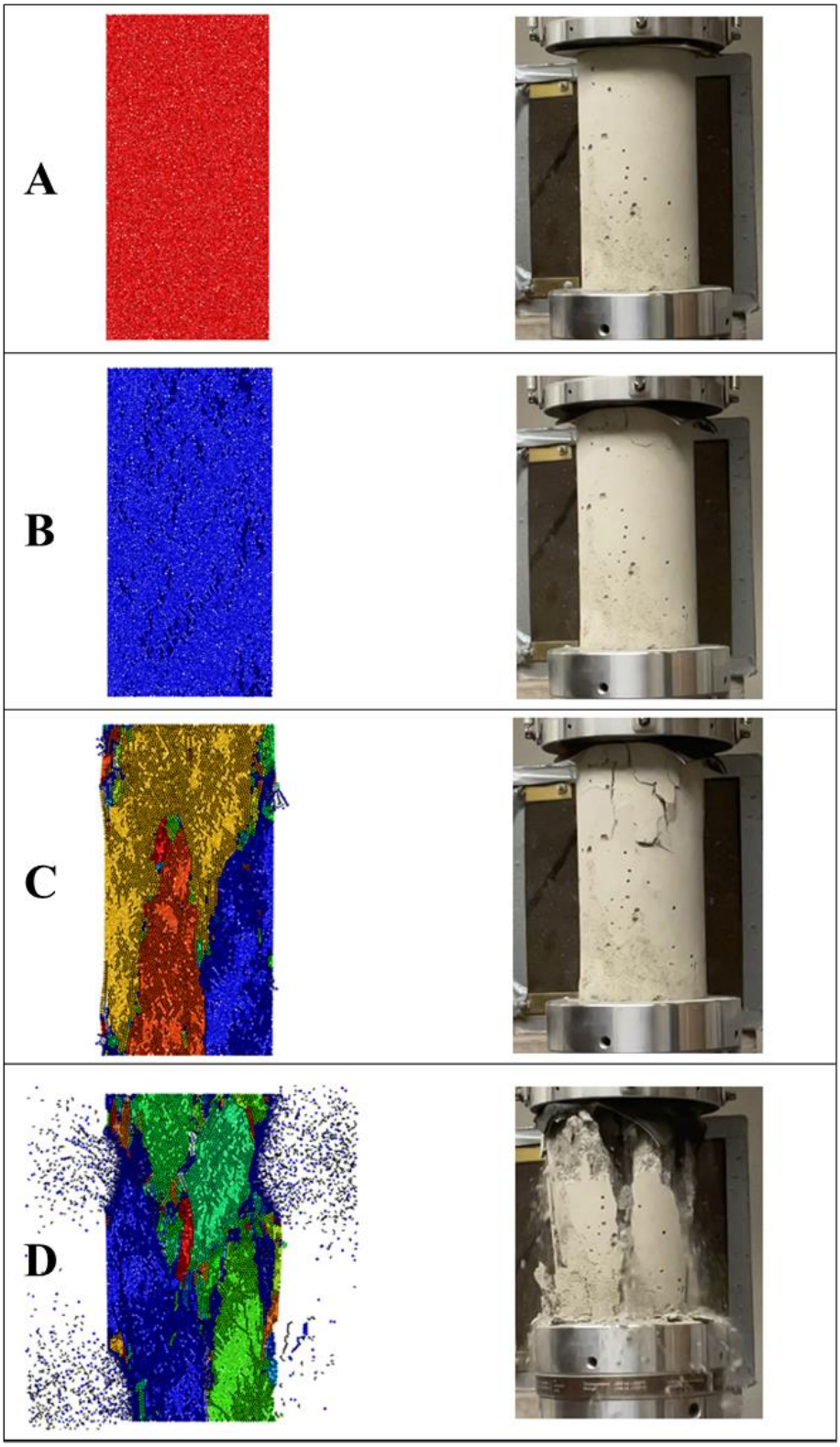

Figure 3.18 Microcrack and fragment generation during compressive simulation (left) in comparison to laboratory compressive tests (right).

3.5 Conclusions

1. Iteration can match material properties in PFC numerical simulations without obtaining equations to correlate laboratory properties and bond properties. Using statistical analysis to generate correlated equations imposes several constraints, such as the ball radius, ball density, and the bond gap across all tests. For example, a change in ball radius changes the material's response in the simulation.

2. The iterative procedure is evaluated by analyzing the impact and degree of influence of 108 simulated samples obtained through uniaxial compressive and direct tension simulations. When performing an iterative calibration procedure, start with the normal-to-shear stiffness ratio (kratio) and bond tensile strength (fj_ten), followed by the effective modulus (emod) and flat-joint cohesion (fj_coh). Bond cohesion should be the last step because it has the least effect on the properties of other materials.

Chapter 4: The Applications of PFC2D on Rock

The PFC program can generate homogeneous materials by specifying a single bond parameter or heterogeneous materials by specifying multiple bond parameters to indicate the ability of each mineral type to withstand different stress. This program has the advantage of monitoring the development of microcracks, but the development of microcracks and fractures during compressive testing in the laboratory is difficult to observe due to the device's limited capability to monitor microfractures, which can develop rapidly. However, by examining the transitional behavior of bonded and unbonded conditions, PFC simulations can use this analysis to predict microcracks development in every simulation. As described in Chapter 2, section 2.4.2, contact between two balls breaks if the bond stress on each element reaches the bond strength. These stresses may be tensile acting perpendicular to the element's surface or shear acting parallel to the interface.

4.1 Microcrack development in homogeneous material

Chapter 3 discusses the process of calibrating the PFC2D's simulated material to match laboratory properties. If the simulated material properties match those in the laboratory, the simulated material should exhibit the same characteristics as an actual sample. Therefore, the stress distribution and crack formation in the laboratory and simulation should be comparable. As a result, the simulation's crack development can be used to explain the laboratory experiment's crack development.

The material properties from iteration nine are used to monitor crack growth during the uniaxial compressive simulation, as shown in Table 3.4. According to the test results shown in Figure 4.1, the increase in the number of cracks is not constant throughout compressive simulations until the material fails. Some regions experience rapid growth, while others see only minor crack development. In the graph, the rate of crack development can be classified into five regions, as demonstrated by the red and blue lines in Figure 4.1.

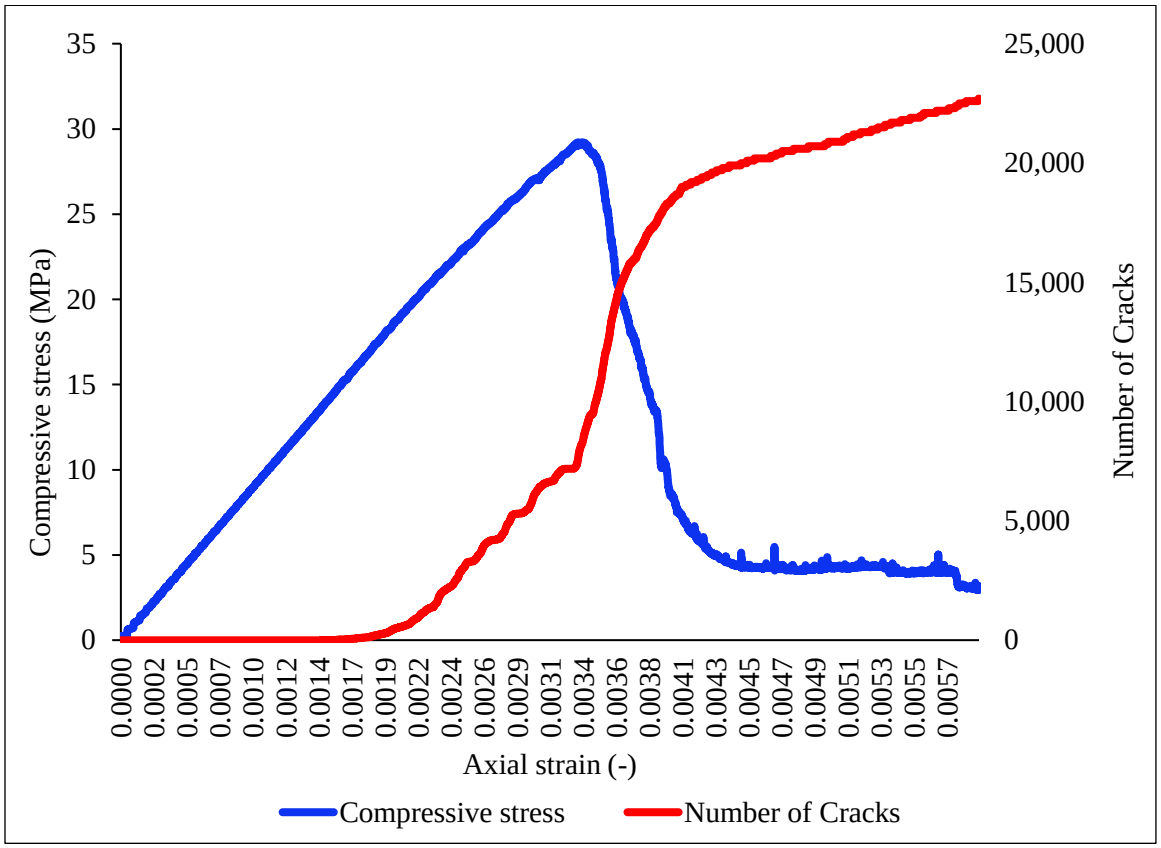

Figure 4.1 Complete stress-strain curve and the number of cracks during compressive simulation of iteration 9.

Region 1: Undamaged stage

This stage is in a linear elastic material. The material in this region is in undamaged condition because this stress does not create a microcrack. According to this simulation, the compressive stress ranges between 0 and approximately 15 MPa, or 50% of its compressive strength. Meanwhile, axial strain encompasses 0.0017, or approximately half of the axial strain that exhibits the ultimate stress. Figure 4.2 shows the region's extent by highlighting it with colored lines.

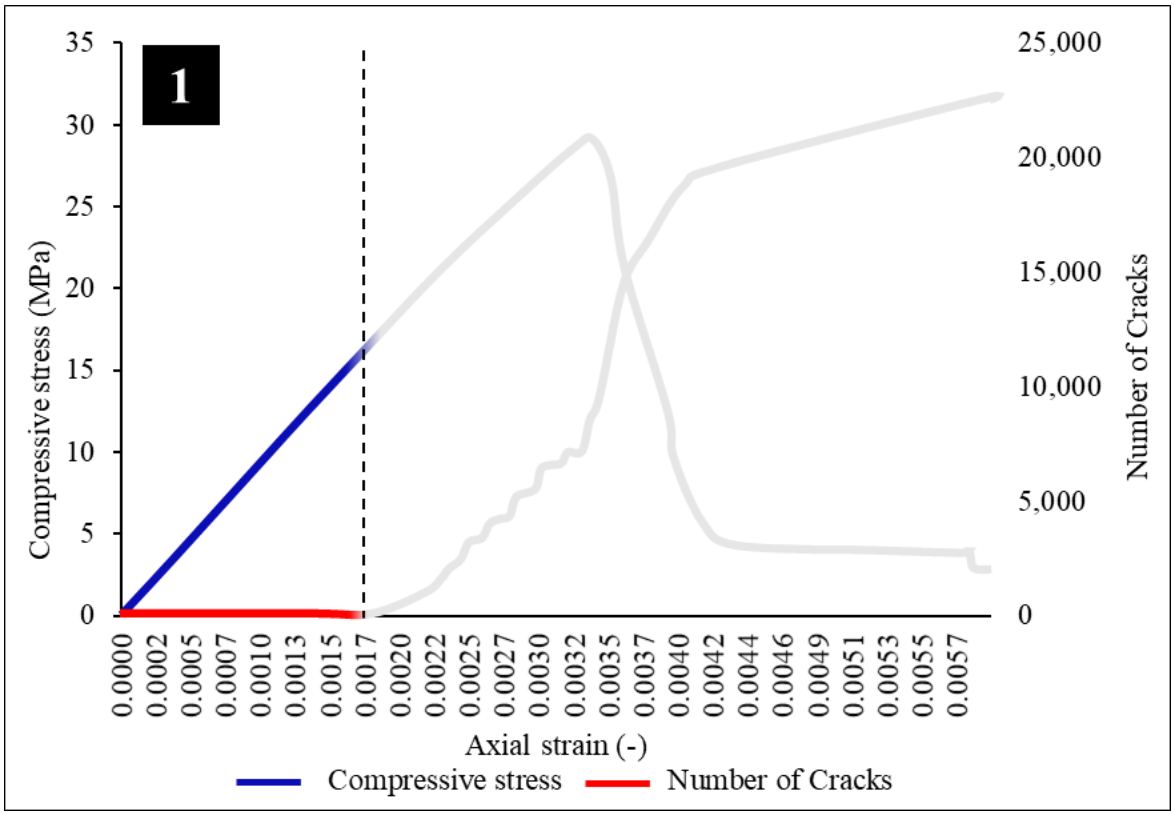

Figure 4.2 Crack development in Region 1 of simulated material from iteration nine.

Region 2: Microcrack development in the linear elastic zone

This stage is in a late stage of linear elastic material, which has the smallest extent comparing to the other four regions. This region is different from Region 1 because the simulated sample is being damaged during the simulation. This region has a relatively low number of cracks. The region's extent is indicated in Figure 4.3 by colored lines. As the stress-stress curve still follows a linear black dash line, it is located in the linear elastic zone.

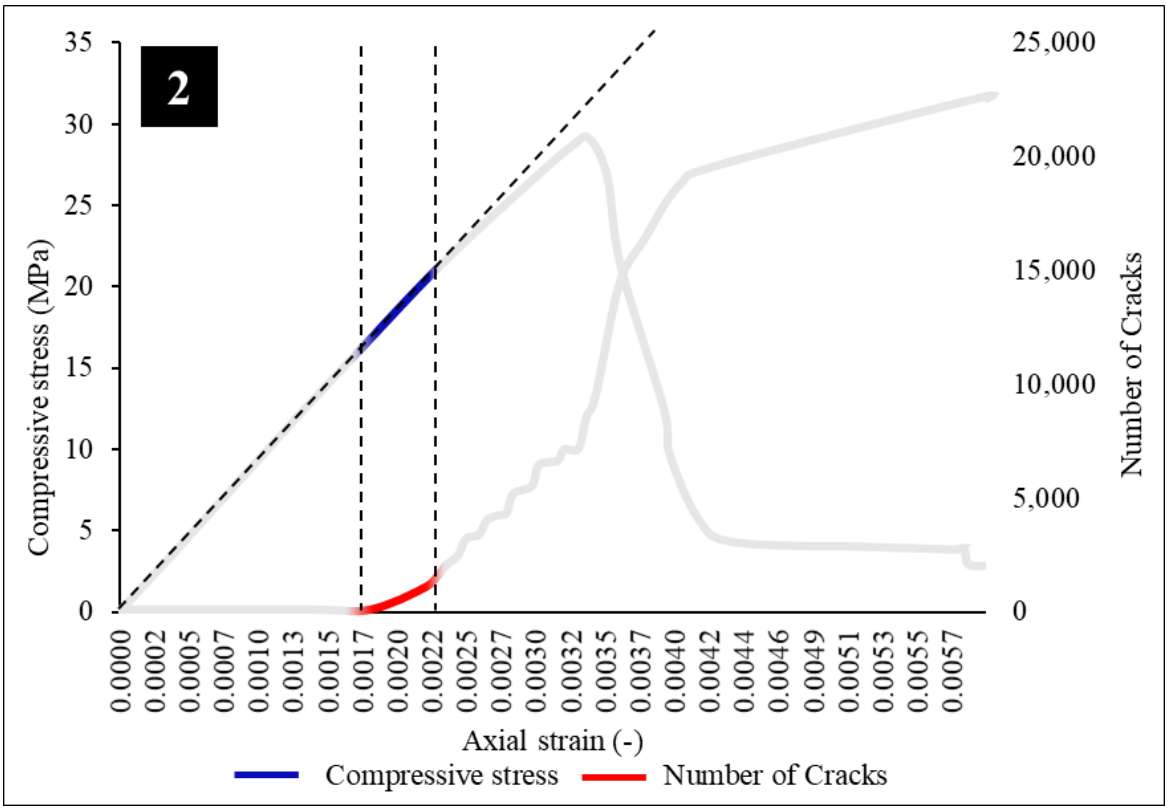

Figure 4.3 Crack development in Region 2 of simulated material from iteration nine.

Region 3: Microcrack development in the strain hardening zone

This stage covers the "strain hardening" zone or plastic zone in which the slope of the stress-strain curve decreases. Although visually observing the change in slope of the stress-stress curve from the simulation is difficult, it can be determined by drawing a linear line to identify off-trend data points (Figure 4.4). Notably, the material's compressive strength is 29.2 MPa, whereas the compressive stress while the material enters this region is 21 MPa or about 70 percent of its strength.

While the material is subjected to compressive stresses ranging from 70% to 100% of its strength, this region does not develop any fragments; however, visuable cracks continue to develop throughout the simulated material (Figure 3.18C & Figure 4.5). Because the material does not have any fragment, stress distribution on all balls in the model is homogenous, as shown in Figure 4.6.

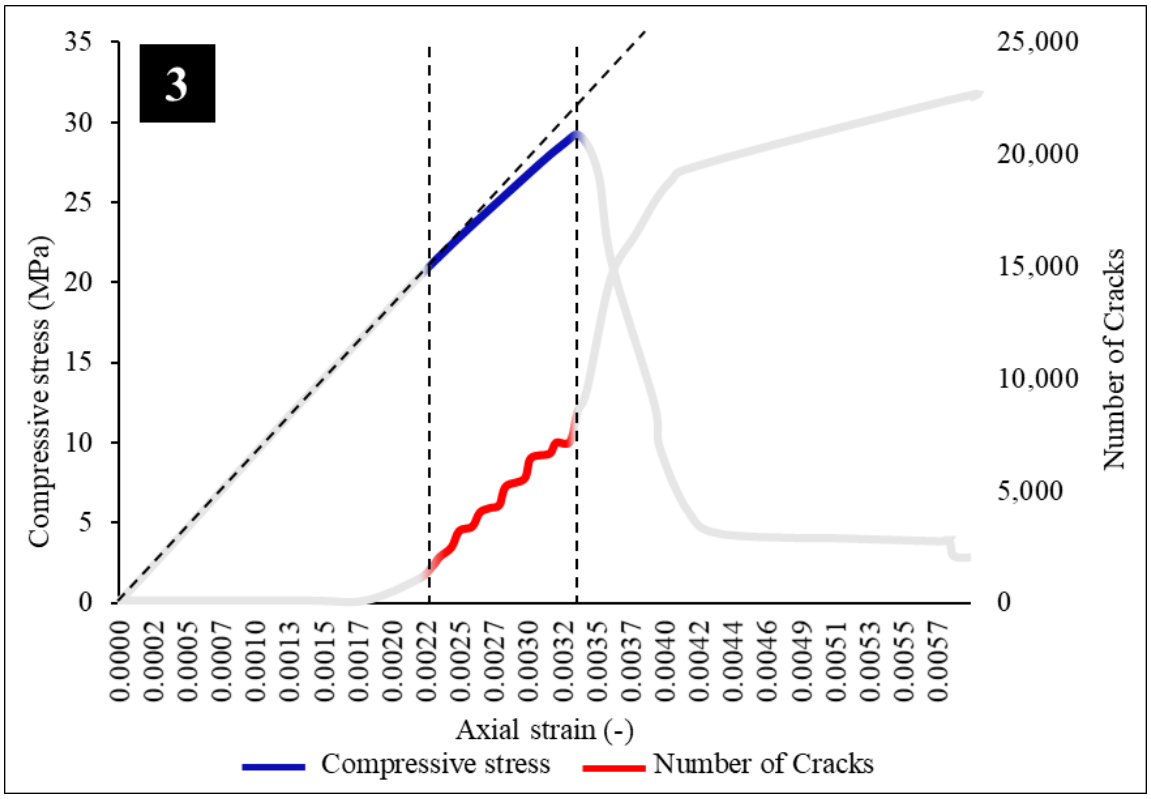

Figure 4.4 Crack development in Region 3 of simulated material from iteration nine.

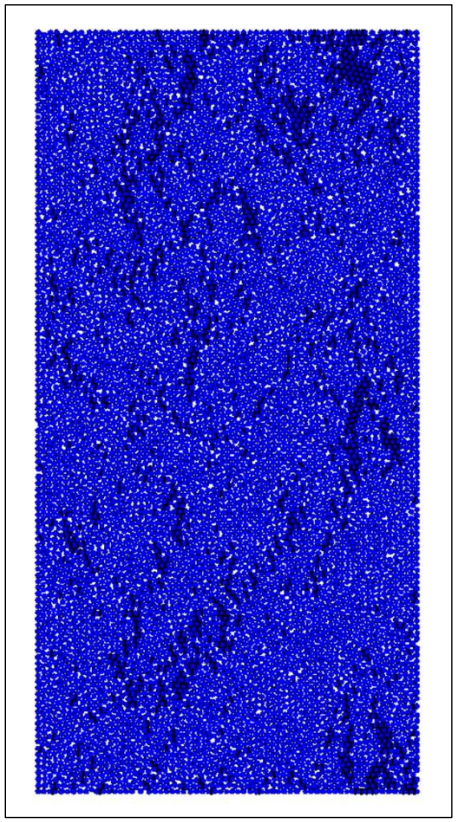

Figure 4.5 Simulated sample during the compressive simulation in Region 3. Black lines indicate cracks.

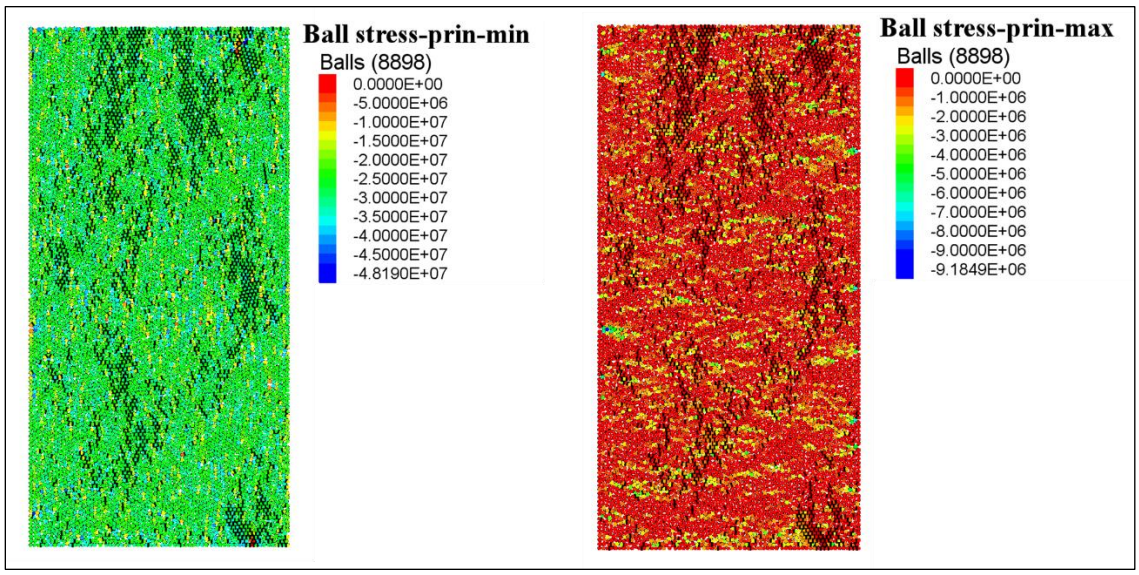

Figure 4.6 Minimum principal stress (left) and Maximum principal stress (right) on each ball in Region 3.

Region 4: Fragmentation

This stage begins when the compressive stress reaches its ultimate strength and ends as the compressive stress decreases just before entering the finite strains zone. Figure 4.7 shows that this region's crack development increases dramatically (Figure 4.8). Because fragmentation creates a discontinuity material, stress distribution on all balls in the model is not equal. As illustrated in Figure 4.9, the distribution of each ball's minimum principal stress (σ_1) is not uniform, but concentrations are along weak zones. Notably, the PFC6.0's sign conventions are as follows: σ_1 denotes minimum principal stress, while σ_3 denotes maximum principal stress.

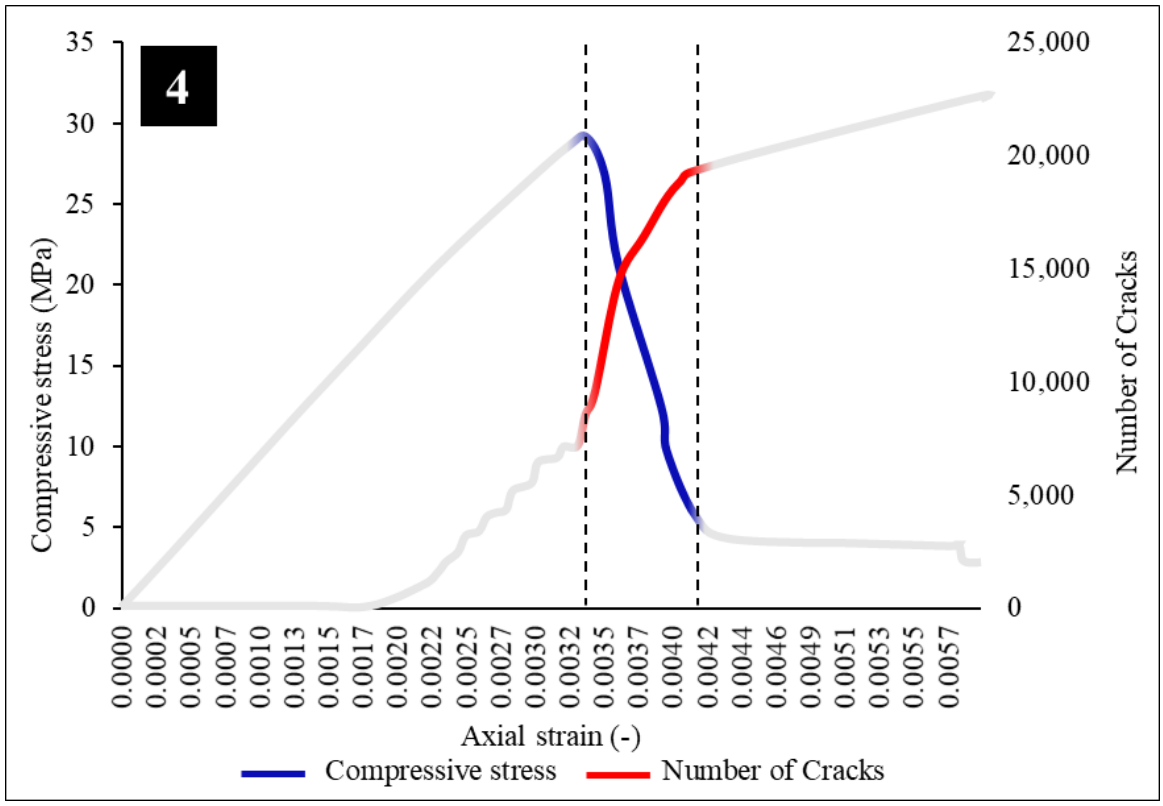

Figure 4.7 Crack development in Region 4 of simulated material from iteration nine.

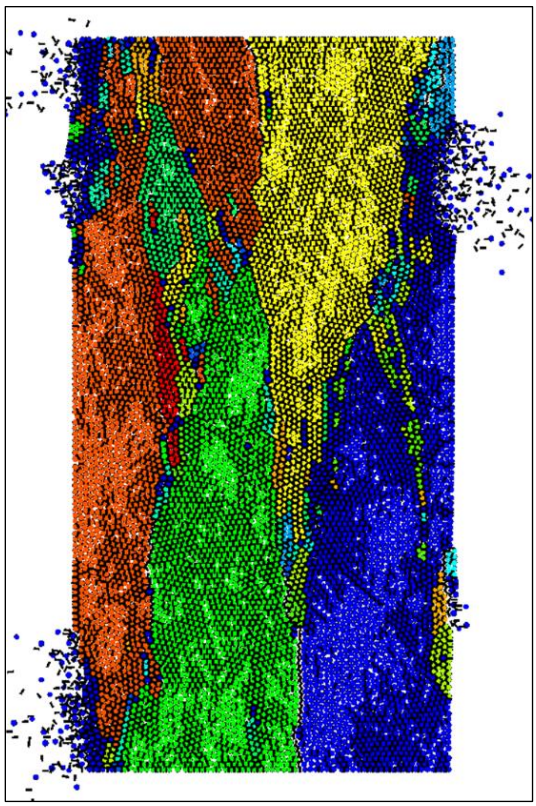

Figure 4.8 Simulated sample during the compressive simulation in Region 4. Black lines indicate cracks, colors indicate fragments.

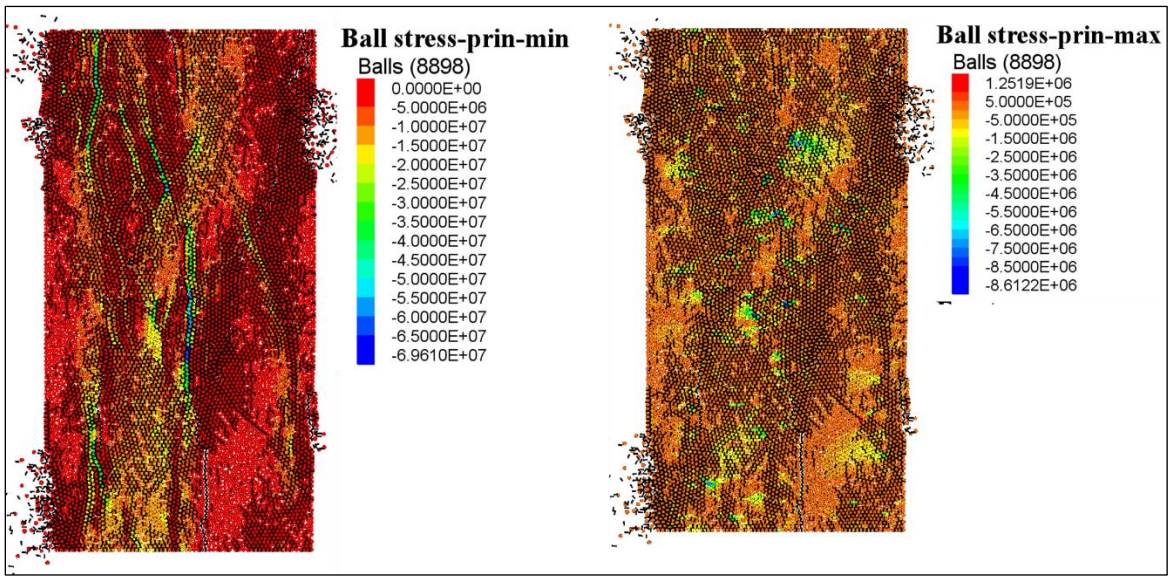

Figure 4.9 Minimum principal stress (left) and Maximum principal stress (right) on each ball in Region 4.

Region 5: Collapsing

The last region illustrated in Figure 4.10 demonstrates that as the axial strain increases, the uniaxial compressive stress remains constant. Even though the compressive stress remains constant throughout loading, the material is damaged and fragmented.

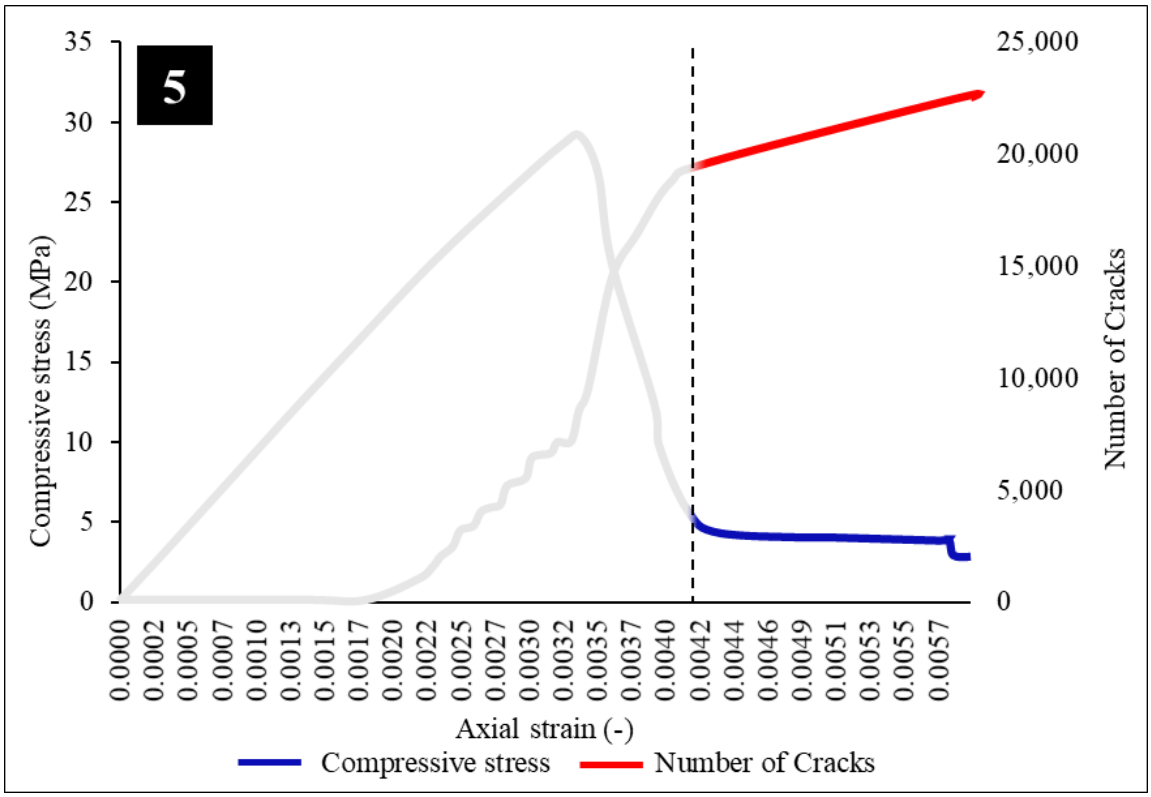

Figure 4.10 Crack development in Region 5 of simulated material from iteration nine.

4.2 Microcrack development of heterogeneous material in the compressive simulation

Certain rocks can have varying degrees of material strength and existing fractures, depending on the proportion of rock-forming minerals present. For example, see Figure 4.11, which shows the great variety of rock-forming minerals under a polarized microscope. Although this rock sample can be found all over the globe, the percentages of minerals content depend on its origin.

This study concentrates on the material's heterogeneity. For the simulation design, there are two different mixtures; the first mixture has a low density, bond tensile strength, and bond cohesion, and the second mixture has a high density, bond tensile strength, and bond cohesion. Table 4.1 lists the properties of two mixtures.

The combination of these mixtures generates seven different materials. Material NO.1 and NO.7 are homogenous materials with 100 percent and 0 percent of Mixture 1. Whereas Materials No. 2 to 6 are heterogeneous materials comprised of two mixtures. Table 4.2 shows the percentage of mixture content in each material.

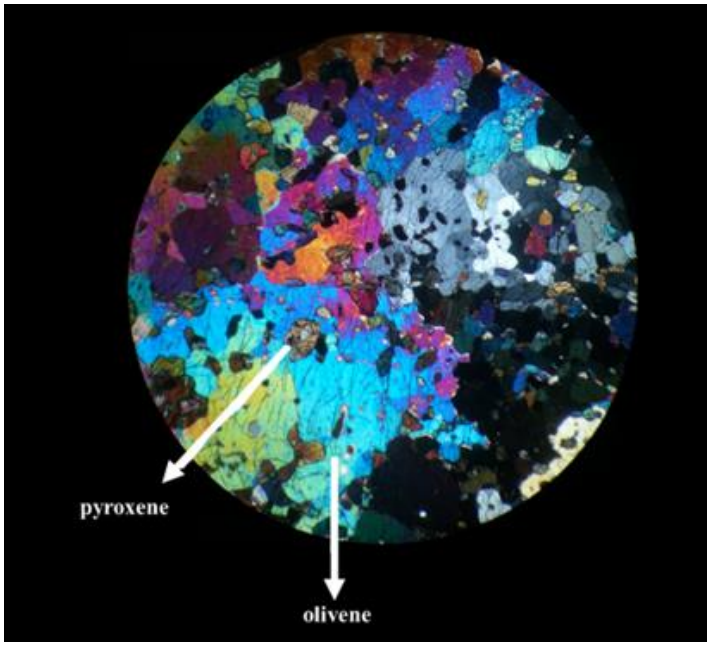

Figure 4.11 Eclogite under polarized microscope.

Table 4.1 Mixture bond's properties of heterogenous material study.

Properties	Mixture 1	Mixture 2
Ball radius (m)	0.0007 - 0.009	
Ball density (kg/m^3)	2245	2700
Emod (Pa)	8.10E+09	20.00E+09
fj_ten (Pa)	4.52E+06	15.00E+06
fj_coh (Pa)	1.46E+07	2.00E+07

Table 4.2 Material mixture content in the heterogeneous material study.

Material number	Mixture 1 (%)	Mixture 2 (%)
1	100.00	0
2	94.44	5.56
3	72.22	27.78
4	50.00	50.00
5	27.78	72.22
6	5.56	94.44
7	0	100.00

According to seven simulations, the uniaxial compressive strength varies proportionally with the mixture content, as illustrated in Figure 4.12. Figure 4.13 illustrates the stress-strain curves of seven simulations. Material NO.1, shown in the purple line, starts cracking when the axial strain is 0.0017 m/m, whereas Material NO.7, shown in the red line, starts cracking when the axial strain is 0.0023 m/m. However, some heterogeneous materials, particularly Material

NO.3, shown in light blue, develop a strain hardening or plastic zone before homogeneous materials, and this zone of Materials NO.3 is wider than those of homogeneous materials, resulting in the material developing microfracture earlier homogeneous materials at an axial strain of 0.0011 m/m.

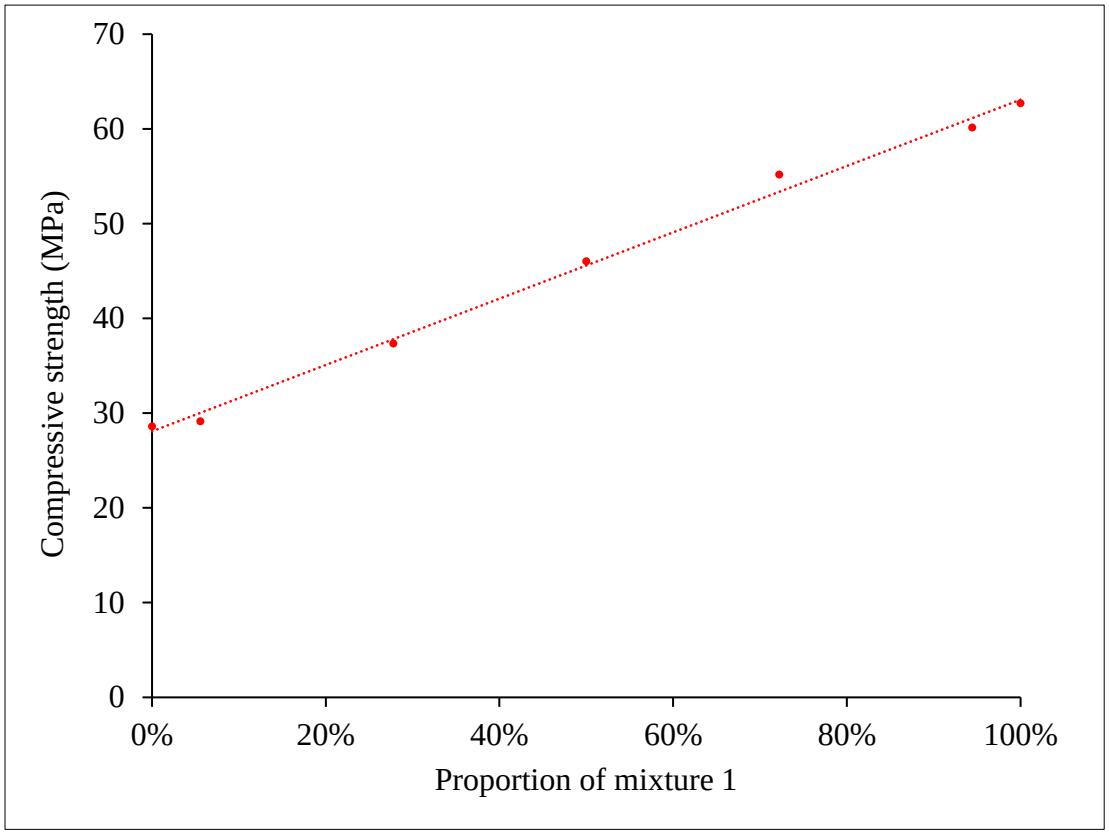

Figure 4.12 Uniaxial compressive strength vs. the percentage of mixture 1.

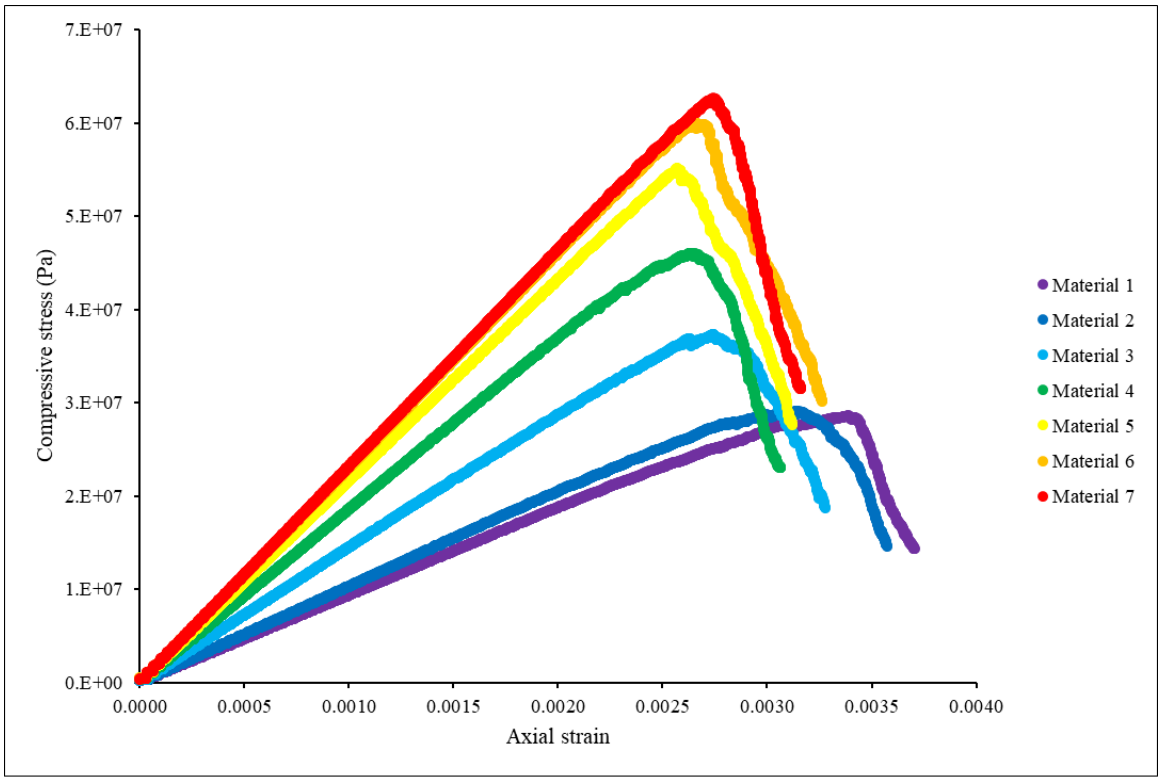

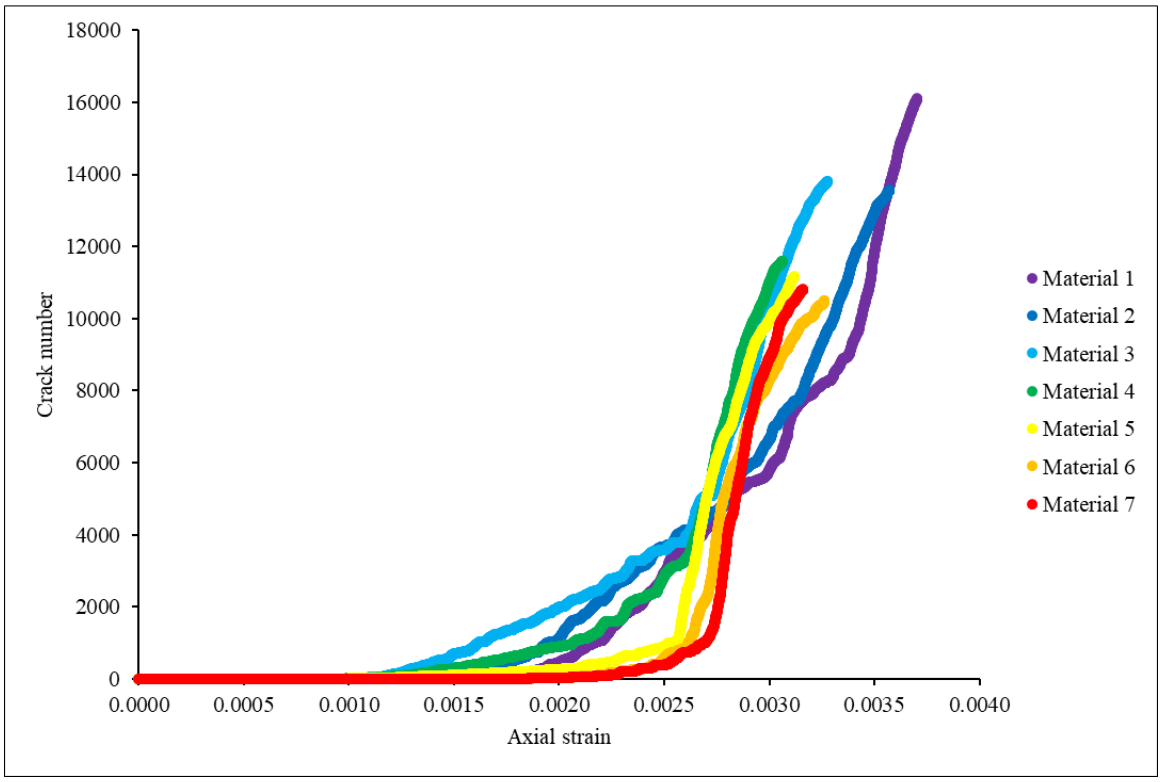

Figure 4.13 Stress-strain curves and crack development of seven materials.

Certain materials exhibit side fractures at the top or bottom (NO.1 and NO.7). However, some materials (NO.2, NO.3, and NO.6) exhibit diagonal fracture cracking through the ends, while others (NO.4 and NO.5) are undefined. Seven sample failures are illustrated in Figure 4.14 when they reach their compressive strength, and the stress drops to 50% of its strength.

As can be seen, neither the crack development nor the fracture pattern of the seven samples is an identical pattern. Some heterogeneous materials start cracking before homogenous materials; some heterogeneous materials have diagonal fracture patterns, while other materials have side fractures at the top or bottom pattern. Therefore, the prediction of damage or the analysis of fragmentation in heterogeneous materials is challenging when using an analytical method. For instance, generating equations to study the relationship between the stress-strain curve and the crack development-strain curve of heterogeneous materials appears impractical. On the other hand, the problem might easily be solved by utilizing DEM.

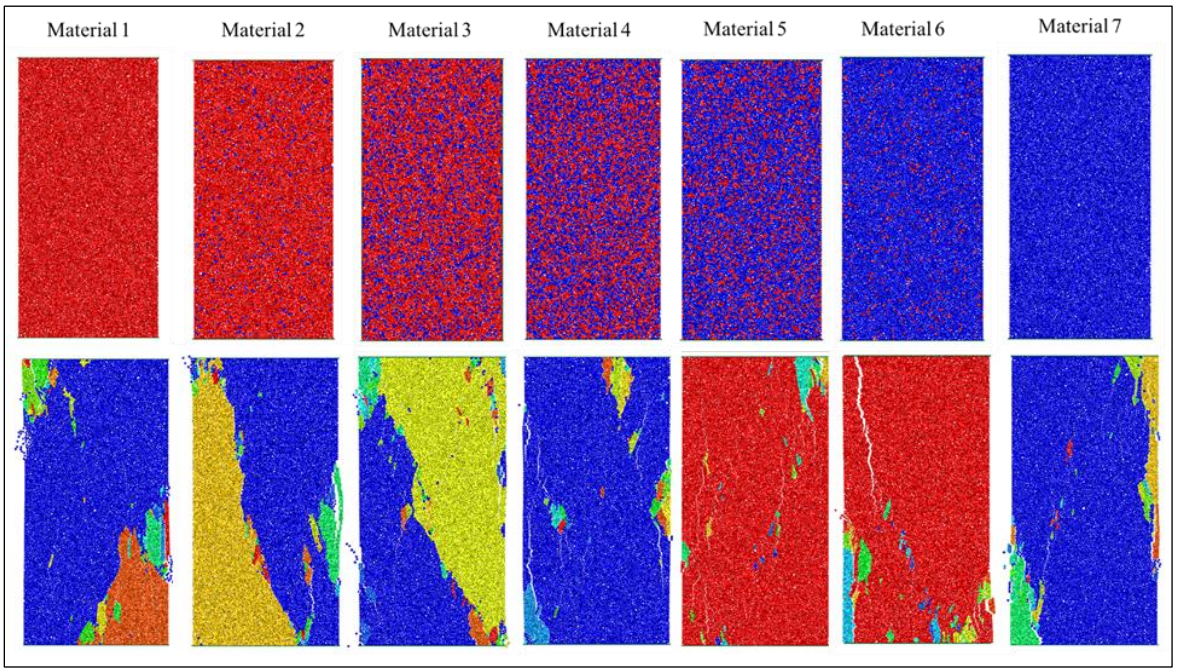

Figure 4.14 The amount of mixture one shows in red balls and mixture two shows in blue balls (top), and fracture pattern of materials, the color indicates each fragment (bottom).

4.3 Influence of lineation's dip angle

Inclusions in volcanic rock, bedding planes in sedimentary rock, foliations in metamorphic rock, or even fracture sets can cause anisotropy in a rock mass. This anisotropy could affect the rock strength regarding stress direction. For example, in the tunneling excavation project, the stress field, radial (σ_r) and tangential (σ_θ), surrounding the open hole are not the same direction, but it depends on the location of the open hole as shown in Figure 4.15. As a result, the principal direction of stress acting on the lineation of the rock varies between 0 and 90 degrees. In the laboratory, determining the rock strength at various angles between the principal stress and the lineation plane can be challenging. To investigate the variation in rock strength, we must collect numerous samples with lineation inclinations ranging from 0 to 90 degrees. These difficulties could become when:

1. There are a limited number of rock specimens. If engineers could not obtain enough rock samples covering an inclination of 0 to 90 degrees, they cannot see the variation in its strength.

2. Some rocks have comparatively large lineation than the background rock, such as interlayered bedding of sandstone and shale, boudinage in gneisses. If the sample to be collected is large, the hydraulic compression device cannot perform the test.

3. Certain rocks, such as highly fractured rock or mica schist with schistosity foliation, have many weak interfaces. Therefore, obtaining a specimen in good condition for the test is difficult.

Therefore, this section uses PFC6.0 to investigate the variation of the compressive strength of rocks containing lineation due to different angles of the maximum principal stress.

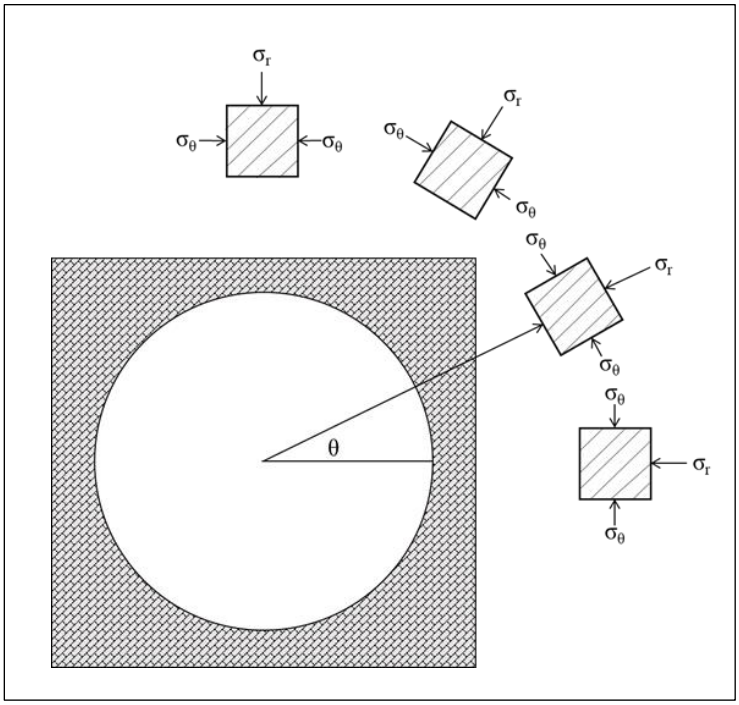

Figure 4.15 Tangential stress and radius stress directions around a circular tunnel.

4.3.1 Methodology to create samples.

In this study, each sample contains two different types of material, which are matrix and inclusion. The bond properties assigned to the matrix are higher than the inclusion. The author specifies exaggeratedly low bond properties for inclusions, as shown in Table 7, to maximize heterogeneity and anisotropy in materials. The inclusions are rod in shape and uniform in size.

Table 4.3 Bond properties of the matrix and inclusions.

Properties	**Matrix**	**Inclusion**
density (kg/m^3)	2245	2700
emod (Pa)	8.10E+09	8.10E+10
fj_ten (Pa)	2.00E+06	5.00E+05
fj_coh (Pa)	8.00E+06	3.00E+05
fj_fric	0.50	0.57
krat	2.50	2.50

The study generates ten samples with a 10-degree increment from 0 to 90 degrees. The term "0-degree angle" refers to the angle between the average orientation of inclusions and the maximum principal stress (or loading direction) is 0 degree, whereas "90-degree angle" refers to the average orientation of the inclusions and the maximum principal stress is 90 degrees. Table 4.4 shows the assigned orientation degree on each sample number, and Figure 4.16 illustrates ten samples with inclusions graphically; dark blue indicates matrix, while red indicates inclusions.

The uniaxial compressive simulations of ten samples are halted when the compressive stress passes the uniaxial compressive strength and drops to 70 percent of its strength.

Table 4.4 Orientation angle on each sample.

Sample NO.	1	2	3	4	5	6	7	8	9	10
Orientation angle (degree)	0	10	20	30	40	50	60	70	80	90

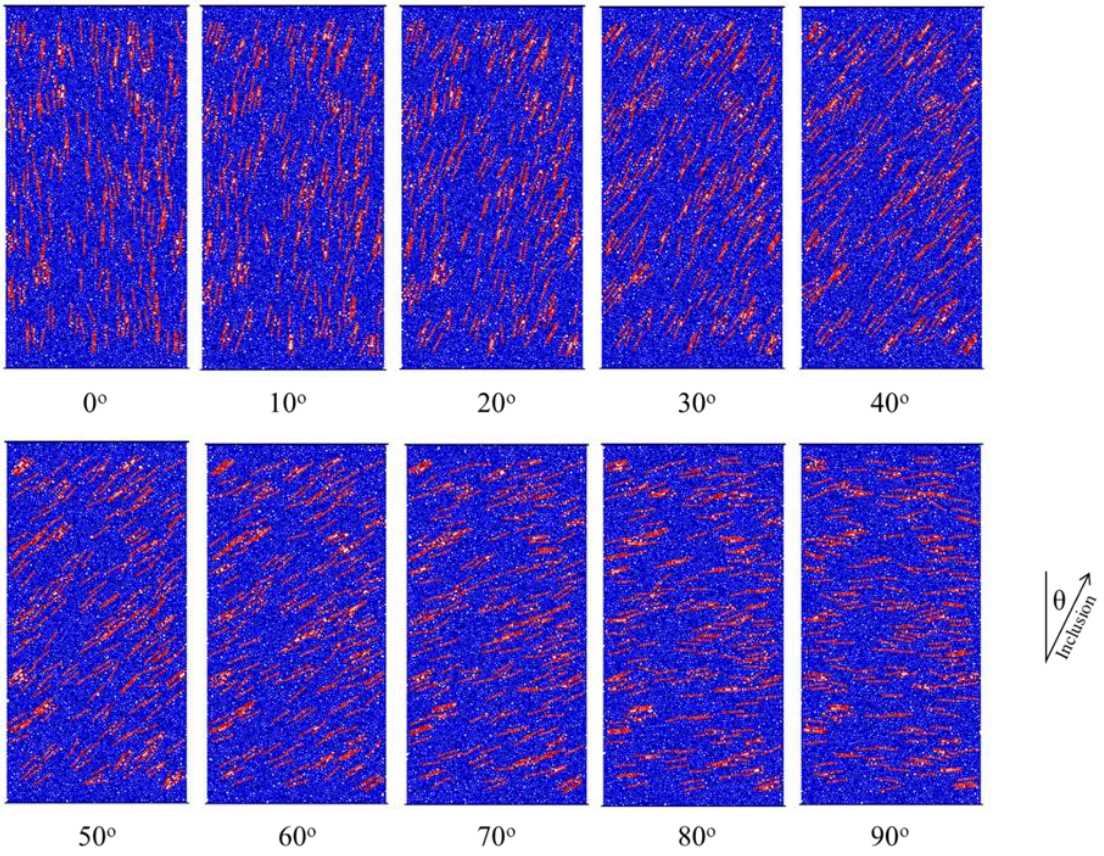

Figure 4.16 Samples to be stimulated to investigate variation in compressive strength.

4.3.2 Simulation results

The simulations show that the compressive strength depends on the inclusions' orientation, as demonstrated by the simulation results in Figure 4.17. In this case, the material with inclusions oriented 90 degrees to the maximum principal stress has the highest compressive strength at approximately 10 MPa. According to Figure 4.17, the compressive strength decreases to approximately 5 MPa when the inclusions of the material orient about 30 degrees to the maximum principal stress. As shown, the uniaxial compressive strength is the lowest at this angle, 30 degrees. Interestingly, the compressive strength reduces approximately 50%. The uniaxial compressive strength increases when the inclusion orientation angle is less than 30 degrees to the maximum principal stress. The samples after the compressive stress drop to 70% of their strength are shown in Figure 4.18.

The stress-strain curves from all simulations shown in Figure 4.19 demonstrate that the axial strain they reach compressive strength varies significantly. The compressive stress-strain curve of materials with 90 degrees-oriented inclusions (black line) has the steepest slope, indicating the highest modulus. In contrast, a material with 30 degrees-oriented inclusions (dark green) has the gentlest slope, indicating the lowest modulus.

Figure 4.19 illustrates the crack development process for each material. Unlike homogeneous material, most of the crack development occurs where the stress-strain curve decreases substantially. However, in this simulation, all samples' crack development curves are completely different from those for homogeneous materials discussed in Chapter 4, section 4.1. The crack growth rate accelerates significantly during the initial loading state because the inclusion properties are significantly weaker than the matrix. As a result, the balls that generate inclusion are damaged first. When the compressive stress increases until it reaches the matrix bond strength, the matrix with a stronger bond strength will be damaged.

Since all crack development trendlines follow the same path, while the compressive stress-strain curves are not identical. The method of determining the crack development of materials containing inclusions by observing the slope of the compressive stress-strain curve may be invalid. Moreover, the orientation of the major microcracks in the simulated samples appears to be random, except for materials with an 80- or 90-degree inclusion orientation, which have the major crack orientation direction at 0 or 180 degrees (or 90 degrees in dipping direction), as shown in Figure 4.20.

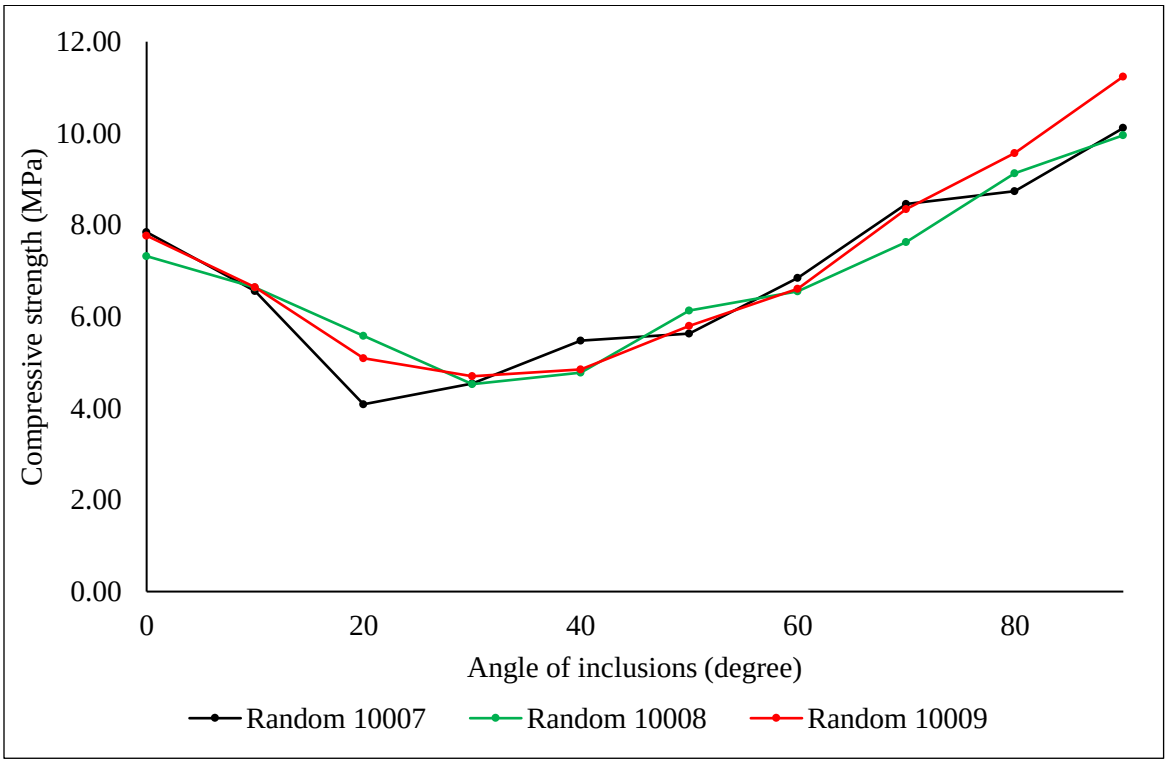

Figure 4.17 Compressive strength versus the orientation angle of inclusions.

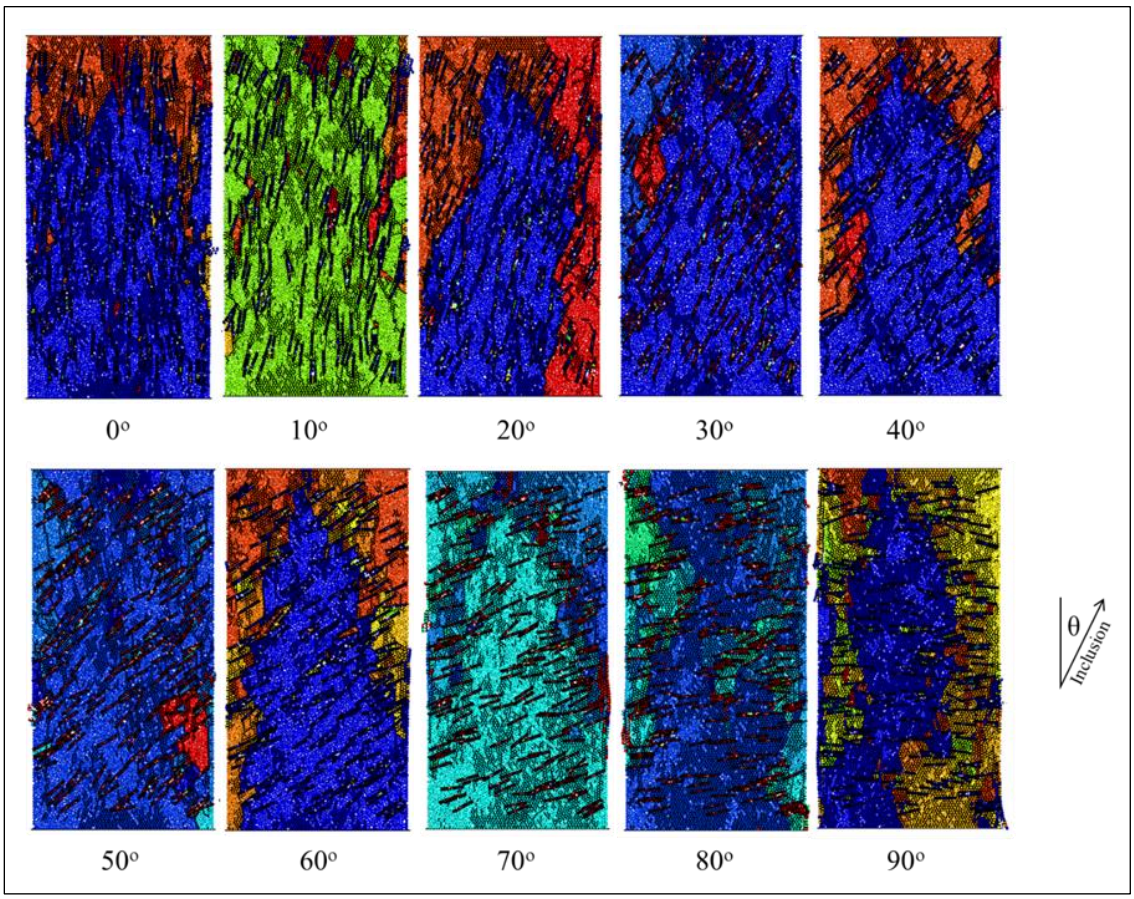

Figure 4.18 Samples after the compressive stress drop to 70% of its strength, black lines indicate fractures.

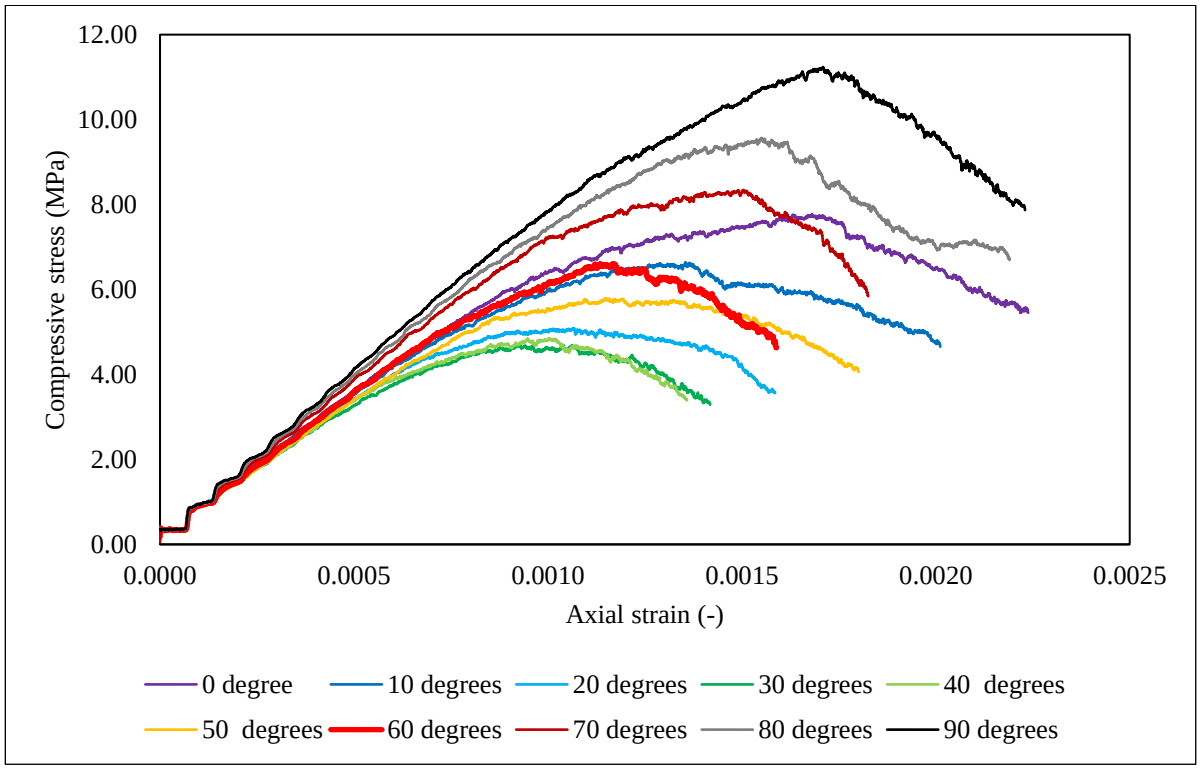

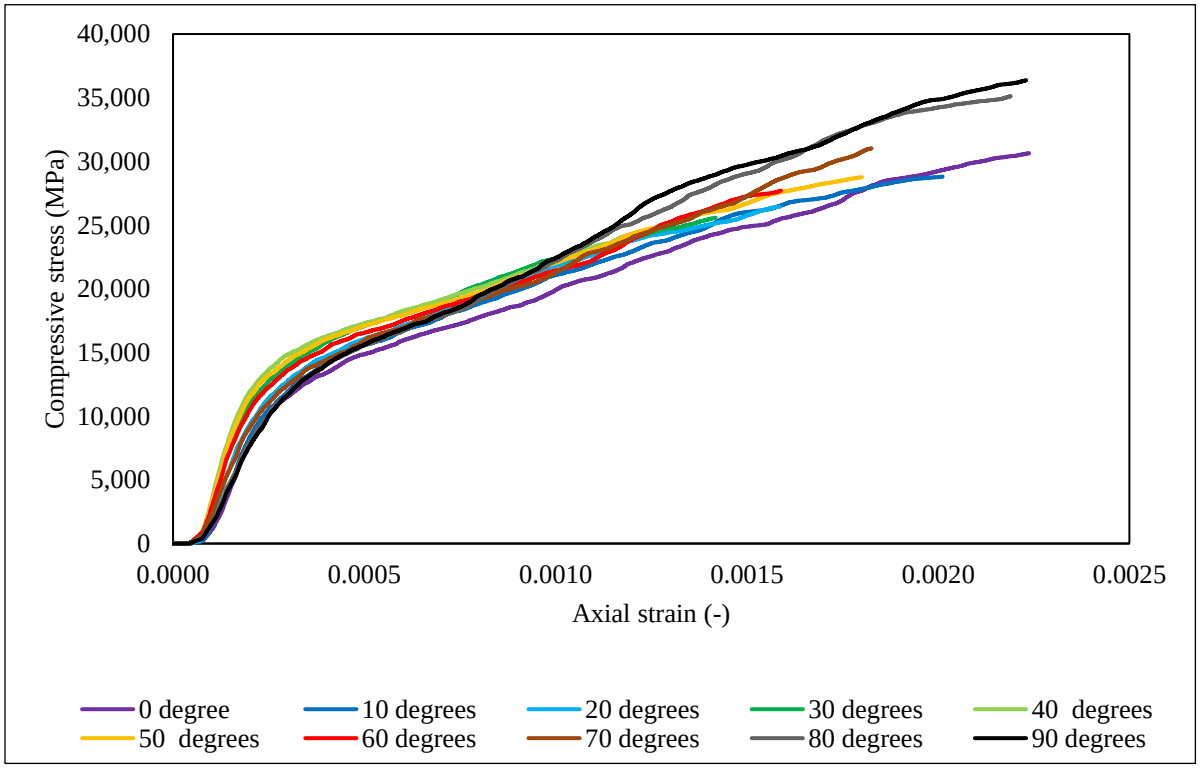

Figure 4.19 The complete stress-strain curves and crack development of the materials.

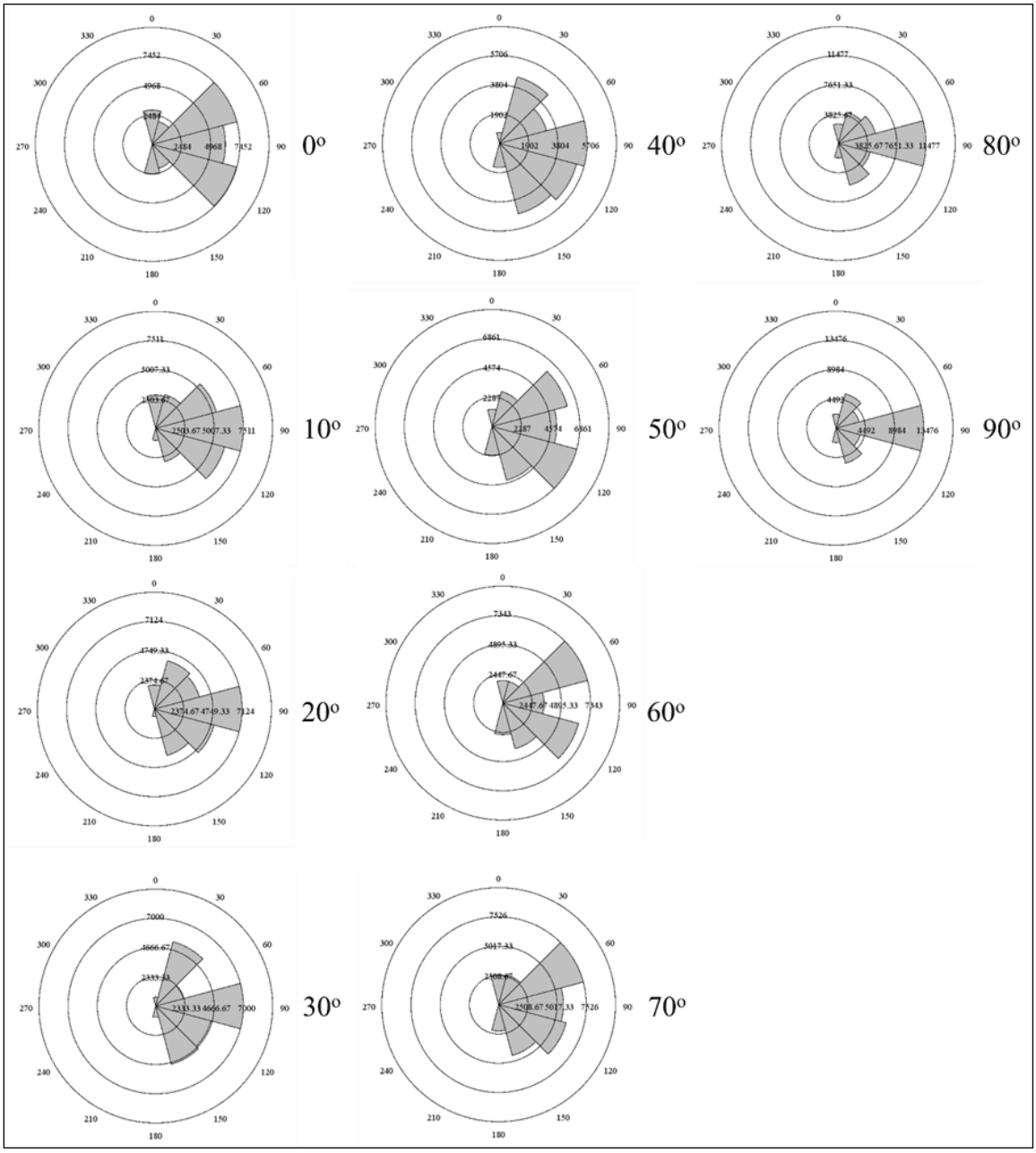

Figure 4.20 Fracture rosette of materials containing inclusions; the number indicates the angle of the inclusions' orientation.

4.4 Conclusions

1. PFC2D is a useful tool for rock mechanics' study. By assigning the appropriate bond properties, it is possible to demonstrate material behavior that cannot be measured directly from the laboratory experiment. Bond breakage in the PFC2D can be used to observe and predict crack development.

2. The simulations demonstrate that the compressive strength of heterogeneous materials varies proportionally with the mixture content.

3. Predicting the growth of damage or the number of cracks in heterogeneous materials is not as straightforward as homogeneous materials because some heterogeneous simulated materials start cracking before homogenous materials.

4. The material's lineation is not constant in compressive strength but varies according to the direction of the maximum principal stress and the material's lineation orientation. Compressive strength is the lowest when lineation acts at a 30-degree angle to the maximum principal stress direction.

5. Not only are differences in compressive strength caused by the direction of the maximum principal stress and the material's lineation orientation, but axial strain (displacement) and Young's modulus also depend on the orientation.

6. Crack development trend of heterogeneous materials could not be predicted by the stress-strain curve, especially the materials that exhibit the lineation.

Chapter 5: Summary, Conclusions, and Recommendations

5.1 Summary

In this study, a flat-joint, built-in, contact model is used to create granular materials. There are four bond parameters to investigate the influence on the macro properties. These are (1) Normal-to-shear stiffness ratio, (2) Effective modulus, (3) Bond tensile strength, and (4) Bond Cohesion. The controlled parameters of the study are ball density, bond friction coefficient, and bond frictional angle. The sample size for the parametric study is 5 centimeters in width and 10 centimeters in height. The sample contains balls with a uniformly distributed radius between 0.3 and 0.4 millimeters, resulting in 11606 balls in the model.

The combination of four bond properties creates 108 different samples. These samples are used to perform uniaxial compressive and tension simulations. Thus, there are a total of 216 simulations in this study. During each compressive simulation, the compressive strength, Young's modulus, and Poisson's ratio of material are monitored. Whereas the tensile strength of a material is monitored in direct tension simulations. Each simulation computation takes about 2-4 hours, depending on micro parameter values assigned to the model. All simulations were performed on a 2020 workstation with an i-7 2.70 GHz Intel CPU, 16.0 GB RAM, and an NVIDIA Quadro T2000 GPU.

The iterative procedure provided in this study is based on the observation of 216 simulations. Additionally, this study provides the crack development study of homogenous material during the compressive simulation in each region, such as linear and nonlinear zones. Moreover, this research extends the compressive simulation study from homogenous materials to heterogeneous materials for randomly distributed particle materials and embedded lineament inclusion materials.

5.2 Conclusions

At the completion of this study, the following conclusions may be made:

1. The iterative procedure provided in this study can effectively simulate the macro behavior. The macro properties obtained from the PFC2D are similar to material properties obtained from laboratory tests.

2. The optimized calibration order for adjusting the input bond parameters should follow the preferred sequence by adjusting: (a) the normal-to-shear stiffness ratio (kratio) to match the material's Poisson ratio, (b) bond tensile strength (fj_ten) to match the material's tensile strength, (c) effective modulus (emod) to match Young's modulus, (d) bond cohesion (fj_coh) to match the material's compressive strength.

3. The cracking of the material can be predicted once the sample is calibrated successfully.

4. The heterogeneous material study shows that the compressive strength changes proportionally for mixed materials.

5. Successfully investigated the influence of lineations. The results show that inclination significantly affects the compressive strength, ultimate strain, and Young's modulus of the materials considered in this study.

5.3 Recommendations

For further research, the following recommendation should be considered:

1. Run biaxial compressive simulations on the material to determine its Mohr-Coulomb criterion and determine the friction angle of the simulated materials. The friction angle of such material is critical for simulating a model in a confined space, such as an underground excavation because the material's shear strength increases with confining pressure.

2. Utilize PFC2D's Discrete Fracture Network (DFN) to generate more realistic rocks for anisotropic material generation. DFN creates the sample to have weak surfaces such as cleavages, fractures, joint sets, and bedding planes. DFN is advantageous when examining fracture patterns because if we use a homogeneous simulated sample to study crack growth patterns in heterogeneous materials.
3. Conduct a study in a 3-Dimensional domain using PFC3D.

References

American Society for Testing and Materials & ILI (Index London Inc.). (2005). Standard Test Method for Compressive Strength of Cylindrical Concrete Specimens. American Society Testing & Materials (ASTM).

American Society for Testing Materials & American Society for Testing Materials. (2010). Standard Test Method for Splitting Tensile Strength of Cylindrical Concrete Specimens. ASTM International.

Brady, B. H. G., & Brown, E. T. (2004). Rock Mechanics: For underground mining (3rd ed.). Springer.

Chen, P. Y. (2016). Effects of Microparameters on Macroparameters of Flat-Jointed Bonded-Particle Materials and Suggestions on Trial-and-Error Method. Geotechnical and Geological Engineering, 35(2), 663–677. https://doi.org/10.1007/s10706-016-0132-5

Cundall, P.A. (1971) A Computer Model for Simulating Progressive Large Scale Movements in Blocky Rock Systems. Proceedings of the Symposium of the International Society for Rock Mechanics, Society for Rock Mechanics (ISRM), France, II-8.

Cundall, P. A., & Strack, O. D. L. (1979). A discrete numerical model for granular assemblies. Géotechnique, 29(1), 47–65. https://doi.org/10.1680/geot.1979.29.1.47

Ding, X., Zhang, L., Zhu, H., & Zhang, Q. (2013). Effect of Model Scale and Particle Size Distribution on PFC3D Simulation Results. Rock Mechanics and Rock Engineering, 47(6), 2139–2156. https://doi.org/10.1007/s00603-013-0533-1

Itasca (2019). PFC2D (Particle Flow Code in 2 Dimensions), Version 6.0, Minneapolis

Jaeger, J., Cook, N. G., & Zimmerman, R. (2007). Fundamentals of Rock Mechanics (4th ed.). Wiley-Blackwell.

Jing, L., & Stephansson, O. (2007). Fundamentals of Discrete Element Methods for Rock Engineering: Theory and Applications, Developments in Geotechnical Engineering, Volume 85, First Edition. Elsevier Science.

Jung, S., Prisbrey, K., & Wu, G. (1994). Prediction of rock hardness and drillability using acoustic emission signatures during indentation. International Journal of Rock Mechanics and Mining Sciences & Geomechanics Abstracts, 31(5), 561–567. https://doi.org/10.1016/0148-9062(94)90159-7

Kačianauskas, R., Balevičius, R., Markauskas, D., & Maknickas, A. (2006). Discrete Element Method in Simulation of Granular Materials. IUTAM Symposium on Multiscale Problems in Multibody System Contacts, 65–74. https://doi.org/10.1007/978-1-4020-5981-0_7A.

Li, Y. L., & Ma, Z. Y. (2017). A Damaged Constitutive Model for Rock under Dynamic and High Stress State. Shock and Vibration, 2017, 1–6. https://doi.org/10.1155/2017/8329545

Liu, D., He, M., & Cai, M. (2017). A damage model for modeling the complete stress–strain relations of brittle rocks under uniaxial compression. International Journal of Damage Mechanics, 27(7), 1000–1019. https://doi.org/10.1177/1056789517720804

Nemat-Nasser, S., & Horii, H. (1984). Rock failure in compression. International Journal of Engineering Science, 22(8–10), 999–1011. https://doi.org/10.1016/0020-7225(84)90101-0

Plackett, R.L. & Burman, J.P. (1946). The Design of Optimum Multifactorial Experiments. Biometrika 33 (4), pp. 305–25, June, doi:10.1093/biomet/33.4.305

Potyondy, D., & Cundall, P. (2004). A bonded-particle model for rock. International Journal of Rock Mechanics and Mining Sciences, 41(8), 1329–1364. https://doi.org/10.1016/j.ijrmms.2004.09.011

Stacey, T. (1981a). A simple extension strain criterion for fracture of brittle rock. International Journal of Rock Mechanics and Mining Sciences & Geomechanics Abstracts, 18(6), 469–474. https://doi.org/10.1016/0148-9062(81)90511-8

Stacey, T. (1981b). A simple extension strain criterion for fracture of brittle rock. International Journal of Rock Mechanics and Mining Sciences & Geomechanics Abstracts, 18(6), 469–474. https://doi.org/10.1016/0148-9062(81)90511-8

Voyiadjis, G. Z. (1987). Introduction to continuum damage mechanics, L. M. Kachanov, Martinus Nijhoff Publishers, 1986. No. of pages: 135. Price U.S. $39.50. ISBN: 90–247-3319-7. International Journal for Numerical and Analytical Methods in Geomechanics, 11(5), 547. https://doi.org/10.1002/nag.1610110509

Wawersik, W., & Fairhurst, C. (1970). A study of brittle rock fracture in laboratory compression experiments. International Journal of Rock Mechanics and Mining Sciences & Geomechanics Abstracts, 7(5), 561–575. https://doi.org/10.1016/0148-9062(70)90007-0

Wawersik, W. R., & Brace, W. F. (1971). Post-failure behavior of a granite and diabase. Rock Mechanics Felsmechanik Mcanique Des Roches, 3(2), 61–85. https://doi.org/10.1007/bf01239627

Yang, R., Bawden, W., & Katsabanis, P. (1996). A new constitutive model for blast damage. International Journal of Rock Mechanics and Mining Sciences & Geomechanics Abstracts, 33(3), 245–254. https://doi.org/10.1016/0148-9062(95)00064-x

Yoon, J. S., Zang, A., & Stephansson, O. (2012). Simulating fracture and friction of Aue granite under confined asymmetric compressive test using clumped particle model. International Journal of Rock Mechanics and Mining Sciences, 49, 68 – 83.

Zhang, X. P., & Wong, L. N. Y. (2014). Choosing a proper loading rate for bonded-particle model of intact rock. International Journal of Fracture, 189(2), 163–179. https://doi.org/10.1007/s10704-014-9968-y

Appendix A

108 uniaxial compressive and 108 direct tension simulations results

	Bond properties				Calculated material properties			
NO.	Effective modulus (GPa)	Normal-to-shear stiffness ratio	Tensile strength (MPa)	Cohesion (MPa)	Compressive strength (MPa)	Tensile strength (MPa)	Compressive/ Tensile ratio	Modulus (GPa)
1	10	3	2	5	12.6	1.3	9.6	10.30
2	20	3	2	5	10.6	1.3	8.1	20.90
3	30	3	2	5	14.0	1.3	10.6	32.10
4	40	3	2	5	12.8	1.3	9.7	41.00
5	10	2	2	5	13.3	1.4	9.8	11.80
6	20	2	2	5	13.5	1.4	10.0	23.40
7	30	2	2	5	11.7	1.4	8.6	35.60
8	40	2	2	5	13.4	1.4	9.8	47.00
9	10	1	2	5	11.7	1.4	8.3	13.90
10	20	1	2	5	11.9	1.4	8.3	27.70
11	30	1	2	5	11.9	1.5	8.2	41.60
12	40	1	2	5	11.9	1.5	8.1	55.50
13	10	3	4	5	14.7	2.6	5.6	10.90
14	20	3	4	5	15.0	2.6	5.7	21.90
15	30	3	4	5	14.8	2.6	5.6	32.80
16	40	3	4	5	14.7	2.6	5.6	43.70
17	10	2	4	5	15.7	2.7	5.9	11.90
18	20	2	4	5	15.9	2.7	5.9	23.60
19	30	2	4	5	16.1	2.7	6.0	35.50
20	40	2	4	5	15.7	2.7	5.8	47.40
21	10	1	4	5	12.9	2.9	4.5	13.90
22	20	1	4	5	11.9	2.9	4.2	27.70
23	30	1	4	5	11.9	2.8	4.2	41.60
24	40	1	4	5	12.3	2.8	4.3	55.50
25	10	3	6	5	17.3	3.9	4.4	11.00
26	20	3	6	5	17.2	3.9	4.4	21.90
27	30	3	6	5	16.4	3.9	4.2	32.90
28	40	3	6	5	16.4	3.9	4.2	43.80
29	10	2	6	5	16.7	4.0	4.1	11.90

	Bond properties				Calculated material properties			
NO.	Effective modulus (GPa)	Normal-to-shear stiffness ratio	Tensile strength (MPa)	Cohesion (MPa)	Compressive strength (MPa)	Tensile strength (MPa)	Compressive/ Tensile ratio	Modulus (GPa)
30	20	2	6	5	16.7	4.0	4.1	0.00
31	30	2	6	5	16.4	4.0	4.1	35.50
32	40	2	6	5	16.4	4.0	4.1	47.40
33	10	1	6	5	12.9	4.3	3.0	13.90
34	20	1	6	5	12.7	4.3	3.0	27.70
35	30	1	6	5	13.2	4.3	3.1	41.60
36	40	1	6	5	13.3	4.3	3.1	55.50
37	10	3	2	10	18.0	1.3	13.7	10.00
38	20	3	2	10	20.2	1.3	15.4	20.00
39	30	3	2	10	19.9	1.3	15.2	29.60
40	40	3	2	10	18.7	1.3	14.2	39.80
41	10	2	2	10	22.0	1.4	16.3	11.60
42	20	2	2	10	22.3	1.4	16.5	23.00
43	30	2	2	10	20.3	1.4	14.9	34.50
44	40	2	2	10	20.9	1.4	15.2	46.30
45	10	1	2	10	22.8	1.4	16.0	13.80
46	20	1	2	10	23.1	1.4	16.2	27.60
47	30	1	2	10	22.1	1.5	15.2	41.50
48	40	1	2	10	23.1	1.5	15.9	55.20
49	10	3	4	10	24.9	2.6	9.5	10.40
50	20	3	4	10	23.0	2.6	8.8	20.90
51	30	3	4	10	21.6	2.6	8.2	32.70
52	40	3	4	10	23.9	2.6	9.1	42.00
53	10	2	4	10	26.9	2.7	10.0	11.80
54	20	2	4	10	26.4	2.7	9.8	23.60
55	30	2	4	10	25.8	2.7	9.6	35.50
56	40	2	4	10	26.2	2.7	9.7	47.20
57	10	1	4	10	23.6	2.9	8.3	13.90
58	20	1	4	10	23.5	2.9	8.2	30.00
59	30	1	4	10	23.7	2.8	8.3	41.60
60	40	1	4	10	23.7	2.8	8.3	55.40
61	10	3	6	10	26.7	3.9	6.8	10.90
62	20	3	6	10	26.8	3.9	6.8	21.80
63	30	3	6	10	25.8	3.9	6.6	32.80

	Bond properties				Calculated material properties			
NO.	Effective modulus (GPa)	Normal-to-shear stiffness ratio	Tensile strength (MPa)	Cohesion (MPa)	Compressive strength (MPa)	Tensile strength (MPa)	Compressive/ Tensile ratio	Modulus (GPa)
64	40	3	6	10	27.3	3.9	7.0	43.30
65	10	2	6	10	27.7	4.0	6.9	11.90
66	20	2	6	10	28.5	4.0	7.1	23.70
67	30	2	6	10	28.1	4.0	7.0	35.60
68	40	2	6	10	28.0	4.0	6.9	47.40
69	10	1	6	10	24.8	4.3	5.8	13.90
70	20	1	6	10	24.3	4.3	5.7	27.80
71	30	1	6	10	24.2	4.3	5.7	41.60
72	40	1	6	10	24.2	4.3	5.7	55.50
73	10	3	2	15	24.6	1.3	18.8	9.78
74	20	3	2	15	27.0	1.3	20.6	19.50
75	30	3	2	15	27.5	1.3	20.9	29.30
76	40	3	2	15	25.1	1.3	19.0	39.30
77	10	2	2	15	28.1	1.4	20.8	11.30
78	20	2	2	15	30.7	1.4	22.7	22.60
79	30	2	2	15	27.0	1.4	19.8	34.20
80	40	2	2	15	30.3	1.4	22.1	45.10
81	10	1	2	15	28.8	1.4	20.2	13.80
82	20	1	2	15	34.5	1.4	24.2	27.60
83	30	1	2	15	28.3	1.5	19.5	41.50
84	40	1	2	15	31.5	1.5	21.6	55.10
85	10	3	4	15	35.4	2.6	13.6	9.99
86	20	3	4	15	31.6	2.6	12.1	20.30
87	30	3	4	15	31.0	2.6	11.8	30.70
88	40	3	4	15	31.1	2.6	11.9	40.30
89	10	2	4	15	31.5	2.7	11.7	11.70
90	20	2	4	15	36.7	2.7	13.6	23.20
91	30	2	4	15	36.8	2.7	13.6	34.70
92	40	2	4	15	33.4	2.7	12.4	47.10
93	10	1	4	15	34.4	2.9	12.1	13.90
94	20	1	4	15	34.3	2.9	12.0	27.70
95	30	1	4	15	34.4	2.8	12.1	41.50
96	40	1	4	15	29.1	2.8	10.2	55.50
97	10	3	6	15	35.4	3.9	9.1	10.50

	Bond properties				Calculated material properties			
NO.	Effective modulus (GPa)	Normal-to-shear stiffness ratio	Tensile strength (MPa)	Cohesion (MPa)	Compressive strength (MPa)	Tensile strength (MPa)	Compressive/ Tensile ratio	Modulus (GPa)
98	20	3	6	15	37.3	3.9	9.5	20.90
99	30	3	6	15	37.1	3.9	9.5	31.10
100	40	3	6	15	37.0	3.9	9.4	41.10
101	10	2	6	15	40.3	4.0	10.0	11.80
102	20	2	6	15	40.4	4.0	10.0	23.50
103	30	2	6	15	39.0	4.0	9.7	35.40
104	40	2	6	15	39.2	4.0	9.7	47.10
105	10	1	6	15	35.3	4.3	8.3	13.90
106	20	1	6	15	35.3	4.3	8.3	27.80
107	30	1	6	15	35.5	4.3	8.3	41.60
108	40	1	6	15	35.5	4.3	8.3	55.50